Compositional heterogeneity of the ancient Martian crust: Analysis of Ares Vallis bedrock with THEMIS and TES data

A. Deanne Rogers, Philip R. Christensen, and Joshua L. Bandfield
Department of Geological Sciences, Arizona State University, Tempe, Arizona, USA

Received 5 January 2005; revised 27 February 2005; accepted 7 March 2005; published 24 May 2005.

[1] THEMIS multispectral and thermophysical information combined with TES hyperspectral and albedo data is used as a powerful high spectral/spatial resolution tool to investigate the mineralogic heterogeneity of ancient Martian crust exposed in Ares Vallis bedrock. Three major spectral units are present in the upper Ares Vallis region: (1) a regional unit that is composed primarily of a high-silica (Si/O > ~0.35) component, with lesser amounts of plagioclase and pyroxene, and is associated with channel wall rock and surrounding plains; (2) a pyroxene- and olivine-rich rock unit exposed as a ~250 m thick contiguous layer in the wall rock of Ares Vallis, as well as in isolated exposures in the plains outside of the channel; and (3) a unit composed of plagioclase, pyroxene, and lesser high-silica component(s) (Si/O > ~0.35) that primarily occurs as low-albedo sand. The spatial and stratigraphic distribution of these units suggests that the pyroxene- and olivine-enriched unit may be extrusive and/or intrusive in origin, indicating that this region experienced either a single stage or repeated episodes of olivine-enriched magmatism during the first 1.5 Gyr of crust formation. This olivine enrichment may have been caused by a larger degree of mantle partial melting, facilitated by higher mantle temperature, melting from a more depleted mantle source, and/or less olivine fractionation relative to regional rock parent magmas. The olivine-rich unit is similar in thermophysical character to previously published olivine-bearing terrains on Mars, but the derived modal mineralogy consists of >~20% more pyroxene and less plagioclase than those terrains.

Citation: Rogers, A. D., P. R. Christensen, and J. L. Bandfield (2005), Compositional heterogeneity of the ancient Martian crust: Analysis of Ares Vallis bedrock with THEMIS and TES data, *J. Geophys. Res.*, *110*, E05010, doi:10.1029/2005JE002399.

1. Introduction

[2] Previous analyses of Martian surface compositions with Mars Global Surveyor Thermal Emission Spectrometer (TES) data have identified mineralogic diversity in low albedo regions on global and regional scales, including spatial variations in feldspar, pyroxene, glass/phyllosilicate, hematite and olivine abundance [*Bandfield et al.*, 2000a; *Christensen et al.*, 2000a, 2000b, 2001a; *Bandfield*, 2002; *Hamilton et al.*, 2002, 2003; *Ruff and Christensen*, 2002a; *Hoefen et al.*, 2003; *Wyatt et al.*, 2003]. These variations occur in spatially coherent patterns and in some areas can be correlated with distinct terrains [*Bandfield et al.*, 2000a; *Rogers and Christensen*, 2003]. An important area of study regarding the evolution of Martian surface compositions is determination of the degree of compositional variability at local scales. The high spatial resolution of the 2001 Mars Odyssey Thermal Emission Imaging System (THEMIS) (100 m/pixel) allows for compositional mapping on subkilometer scales, permitting lithologic units and stratigraphic relationships to be distinguished [*Christensen et al.*, 2003; *Bandfield et al.*, 2004a; *Hamilton and Christensen*, 2005; *Christensen et al.*, 2005].

0148-0227/05/2005JE002399$09.00

[3] The upper Ares Vallis outflow channel cuts 1–2 km into ancient Noachian and Hesperian rocks [e.g., *Scott and Tanaka*, 1986; *Rotto and Tanaka*, 1995], exposing the stratigraphy and providing important insights into the formation of the early Martian crust. The channel and surrounding areas exhibit high spectral and thermophysical diversity at THEMIS resolution, making this area ideally suited for local-scale mapping of compositional variability. The floor of Ares Vallis exhibits a relatively high thermal inertia (>800 J m^{-2} K^{-1} $s^{-1/2}$) at TES spatial resolution [*Mellon et al.*, 2000; *Jakosky and Mellon*, 2001], and also is a region of high rock abundance [*Christensen*, 1986; *Nowicki and Christensen*, 2003]. The channel was first identified as a compositionally diverse area from spectral analysis of global bedrock locations using THEMIS nighttime and daytime infrared images [*Rogers et al.*, 2003].

[4] The Ares Vallis outflow channel spans ~2000 km in length, 25–65 km in width and ~1200–2000 m in depth. The source regions are Iani, Aram, Hydaspis, and Margaritifer Chaos [*Sharp*, 1973; *Scott and Tanaka*, 1986; *Chapman and Tanaka*, 2002], and the mouth of the channel opens into the plains of Chryse Planitia. The landing site for the 1997 Mars Pathfinder spacecraft is located ~200 km from the mouth of Ares Vallis; this site was chosen with the science goal of sampling a variety of rock types that may

have originated from the southern highlands [e.g., *Golombek et al.*, 1997].

[5] The formation of Ares Vallis and other Martian outflow channels occurred during the late Hesperian to early Amazonian time period [*Tanaka*, 1986; *Rotto and Tanaka*, 1995; *Tanaka et al.*, 2003; *Tanaka et al.*, 2005]. The Ares Vallis channel cuts through Noachian units and Hesperian plains [*Scott and Tanaka*, 1986; *Rotto and Tanaka*, 1995]. It is generally accepted that a catastrophic flooding event initially formed the channel [e.g., *Baker et al.*, 1992]; however, several different mechanisms have been proposed for outflow channel modification, including mass-wasting, glacial, or aeolian processes [e.g., *Baker and Milton*, 1974; *Carr*, 1979; *Cutts and Blasius*, 1981; *Baker et al.*, 1992; *Chapman and Tanaka*, 2002]. It is likely that a combination of these processes have modified the channel since its initial formation [*Chapman and Kargel*, 1999]. The catastrophic event(s) to initially form the channels may have been triggered by magmatic processes [e.g., *Maxwell and Picard*, 1974; *Masursky et al.*, 1977; *Chapman and Tanaka*, 2002].

[6] *Treiman* [1997] recognized layered variations in relative brightness in the Ares Vallis region, generally within 250 m vertical distance from the highland surface through which the channel was eroded, and interpreted these as potential hardpan units of differing cementation mineralogy. He noted that the layers were consistently present in the (unfortunately) incomplete coverage with high-resolution Viking data, and suggested that the Ares Vallis layers may have a common origin with similar layered units in Valles Marineris.

[7] This work presents a detailed analysis of the compositions and geologic features present in the canyon floor, walls, and surrounding plains of the upper Ares Vallis region (using the geographical name designated for this region by *Tanaka et al.* [2005]), as well as the interpreted stratigraphy and geologic history of the area. Ares Vallis incises Noachian and Hesperian layered rock, has large areas that are low-albedo, implying little dust cover, and exhibits high rock abundance, suggesting local bedrock sources are exposed. These characteristics make this region ideal for investigation of compositional heterogeneity of ancient Martian crust with thermal infrared observations. The objectives are to (1) identify the spectrally unique units that are present and characterize their mineralogy; (2) map the distribution and stratigraphy of these units; and (3) discuss the implications of the mineralogic assemblages present and their stratigraphy for the geologic history of the study region.

2. Data and Methods

2.1. MGS Thermal Emission Spectrometer (TES)

[8] The TES instrument provides hyperspectral data at low spatial resolution ($3 \times \sim 8$ km) that are complementary to high spatial resolution THEMIS data for compositional studies. A detailed description of the TES instrument and calibration is given in [*Christensen et al.*, 1992, 2001b]. TES data used in this study were constrained to warm-surface (>255 K) spectra with low emission angles (<30°), within the MGS mapping phase orbits 1–5703. Some orbits within this range contain spectral artifacts, which become increasingly common in the emissivity data from around orbit 5317 onward (see *Bandfield* [2002] or *Hamilton et al.* [2003]). Orbits that contain the spectral artifacts were avoided in this work.

Table 1. End-Members Used in Deconvolution Model

ASU ID	Mineral Name[a]
55	Quartz BUR-4120
43	Microcline BUR-3460
5	Albite WAR-0244
22	Oligoclase WAR-0234
1	Andesine BUR-240
63	Labradorite WAR-4524
177	Bytownite WAR-1384
178	Anorthite BUR-340
28	Actinolite HS-116.4B
30	Enstatite HS-9.4B
6	Bronzite BUR-1920
36	Diopside BUR-1820
164	Augite DSM-AUG01
147	Augite NMNH-119197
145	Hedenbergite manganoan DSM-HED01
8	Forsterite BUR-3720A
38	Forsterite AZ-01
167	Fayalite WAR-RGFAY01
	KI 3115 Fo68 Olivine[b]
	KI 3362 Fo60 Olivine[b]
	KI 3373 Fo35 Olivine[b]
	KI 3008 Fo10 Olivine[b]
25	Biotite BUR-840
29	Phlogopite HS-23.3B
	K-rich Glass[b]
14	Serpentine HS-8.4B
211	Illite granular IMt-2 - 60% blackbody[c]
193	Hectorite solid SCHa-1
197	Ca-montmorillonite solid STx-1
50	Hematite BUR-2600
119	Calcite C40
110	Dolomite C20
81	Anhydrite ML-S9
82	Gypsum ML-S6
	Average high albedo surface[d]

[a]Chemical formula for ASU samples given at http://tes.asu.edu.
[b]Olivine samples provided by V. E. Hamilton and are described by *Morse* [1996]; glass sample described by *Wyatt et al.* [2001].
[c]Blackbody was subtracted from the spectrum to produce comparable spectral contrast to that of other solid clays in the ASU library.
[d]Derived from emission phase function observations with TES by *Bandfield and Smith* [2003].

2.1.1. Linear Deconvolution and End-Member Library Description

[9] This study utilizes the linear deconvolution technique for separating atmospheric components from surface emissivity [*Bandfield et al.*, 2000b; *Smith et al.*, 2000]. Previously isolated atmospheric dust and water ice end-members [*Bandfield et al.*, 2000b], the average Martian high-albedo surface spectrum [*Bandfield and Smith*, 2003], synthetic CO_2 and water vapor spectra [*Bandfield*, 2002], a blackbody spectrum and a set of mineral end-members (Table 1) are used to obtain a linear least squares fit to the measured effective emissivity. The algorithm is similar to that developed by *Ramsey and Christensen* [1998] for determination of mineral abundances from laboratory emission spectra. The output of the algorithm is a set of spectral end-member concentrations and derived surface emissivity [e.g., *Bandfield*, 2002]. Accuracy with this technique relies on high signal to noise and minimal atmospheric dust (extinction $<\sim 0.15$) and ice (extinction $<\sim 0.08$) at the time of data

acquisition. The signal-to-noise ratio is maximized by averaging several spectra (usually 6 or more) over the region of interest; spectra with high atmospheric dust and ice loadings are typically not used for surface emissivity determination, because strong absorptions from these constituents will mask surface absorptions. In this study, some of the surfaces of interest were approximately the same size of a TES pixel (3 × ~8 km) or smaller, therefore the number of TES spectra that were available for averages of each spectral unit were limited (4 to 8 spectra for two of the units). However, confidence in accurate determination of surface emissivity is given by the derived THEMIS surface emissivity for each unit.

[10] For each spectral unit, major chemical oxide weight percentages are calculated from the derived modal mineralogy by the method of [*Hamilton and Christensen*, 2000; *Hamilton et al.*, 2001; *Wyatt et al.*, 2001]. *Wyatt et al.* [2001] determined derived oxide errors of ±5 wt% using this technique for laboratory spectra of terrestrial volcanic rocks with 2 cm^{-1} spectral sampling. *Hamilton et al.* [2001] degraded the rock and mineral end-member spectra of *Wyatt et al.* [2001] to TES spectral resolution and reported the standard deviation of the absolute differences between measured and modeled abundances for each oxide. Derived chemical abundances in this work are rounded to the nearest percent and are reported with the standard deviations defined by *Hamilton et al.* [2001]. Uncertainties are likely to be higher for orbital data. Chemical abundances are used in addition to the modal mineralogy in an effort to classify each identified spectral unit as a particular lithology.

[11] The spectral end-member library used in this work is given in Table 1. The library is similar to that of *Bandfield* [2002], with additional olivine end-members included. Olivine spectra were provided by V. E. Hamilton and the samples are described by *Morse* [1996]. Silica glass spectra were provided by M. B. Wyatt and are described by *Wyatt et al.* [2001]. The other mineral end-members are from the ASU spectral library [*Christensen et al.*, 2000c]. Mineral end-members were selected primarily by the sample purity and also the presence of characteristic spectral features that well-represent the respective mineral group.

[12] Note that obsidian glass (Si-K glass) is spectrally similar to several types of high-silica secondary minerals and coatings, such as phyllosilicates, zeolites, amorphous silica, or palagonitic rinds, in the TES wavelengths used for deconvolution of surface emissivity [*Bandfield*, 2002; *Wyatt and McSween*, 2002; *Kraft et al.*, 2003; *Michalski et al.*, 2003, 2004; *Morris et al.*, 2003; *Ruff*, 2004]. While broadly similar, the position of the fundamental Si-O stretching absorption in all phyllosilicates is shifted to slightly lower wave numbers than obsidian glass [*Koeppen and Hamilton*, 2004; *Michalski et al.*, 2004]. In addition, *Ruff* [2003] demonstrated a lack of long-wavelength (~465 and 530 cm^{-1}) features that are characteristic of phyllosilicates in TES emissivity spectra from low-albedo regions. *Ruff* [2003], *Koeppen and Hamilton* [2004], and *Michalski et al.* [2004] conclude that phyllosilicates are not likely to be a major component of Martian dark regions, consistent with VIS/NIR observations [e.g., *Soderblom*, 1992; *Blaney et al.*, 2003]. Some zeolites also have comparable spectral character to obsidian glass in the thermal infrared [*Ruff*, 2004]. Finally, pure amorphous silica [*Kraft et al.*, 2003; *Michalski et al.*, 2003] and palagonitic rinds [*Morris et al.*, 2003] are similar in spectral character to obsidian glasses in the thermal infrared. Sedimentary silica coatings are a likely alteration product for Martian basalts [*Gooding*, 1992; *Kraft et al.*, 2003; *McLennan*, 2003]. In this study, concentrations of phyllosilicates and glasses that are modeled in deconvolution of TES surface emissivity are combined and reported as a total concentration of "high-silica component(s)," and a Si/O > ~0.35 is implied [after *Michalski et al.*, 2005]. This material should be interpreted as one or a combination of primary glass, amorphous secondary silica, palagonitic rinds, zeolite, or phyllosilicate components, with glass and/or amorphous silica coatings being the most likely components.

2.1.2. Spectral Ratio Technique

[13] An adverse effect of averaging spectra is that small-scale spatial variations in surface mineralogy are more difficult to detect. Therefore, in the present study, spectral ratios are used in addition to linear deconvolution techniques to help isolate unique components in small areas of interest or even a single TES spectrum [*Ruff and Christensen*, 2002b; *Christensen et al.*, 2003; *Ruff*, 2003]. Spectra from a THEMIS IR image can be used to verify the spectral differences between the two surfaces used in the TES ratio.

2.2. The 2001 Mars Odyssey Thermal Emission Imaging System (THEMIS)

2.2.1. THEMIS Instrument Description and Calibration

[14] The THEMIS instrument consists of two multispectral cameras, a 10-band infrared imager with ~100 m/pixel spatial sampling, and a 5-band visible/near-infrared (VIS/NIR) imager with ~18 m/pixel spatial sampling [*Christensen et al.*, 2004a]. The 10 bands of the IR camera are centered at 9 different wavelengths, with an average bandwidth of ~1 μm for each channel. Bands 1 and 2 were designed to have identical filters centered at ~6.8 μm for the purpose of improving the signal-to-noise in this wavelength region. The remaining bands are centered at ~7.9, 8.6, 9.4, 10.2, 11.0, 11.8, 12.6, and 14.9 μm. The visible camera bands cover the wavelength range of 0.425–0.860 μm. A full description of the instrument and calibration is given by [*Christensen et al.*, 2004a].

[15] A number of systematic sources of noise and radiance errors in calibrated radiance images have been identified and characterized by *Christensen et al.* [2004a] and *Bandfield et al.* [2004b]. Time-dependent changes in the detector temperature that introduce up to ±10 DN errors in the along-track direction of an image and small systematic constant radiance offsets are not corrected in the standard THEMIS calibration. Methods of correcting for these errors are described by *Bandfield et al.* [2004b] and are applied to all daytime IR images used in this work. Only the time-dependent temperature changes are corrected in nighttime IR images.

2.2.2. Surface-Atmosphere Separation and Compositional Analysis Techniques

[16] All THEMIS calibrated radiance images contain a constant atmospheric emission contribution. If not corrected, the consequence will be variable effective spectral emissivity from surfaces of different temperatures. A method for removing the atmospheric emission component is described by *Bandfield et al.* [2004b] and is applied to all

daytime IR images used in this work. This method simultaneously removes the systematic calibration radiance offsets that are present in each image (mentioned above).

[17] After correcting for the time-dependent temperature changes and the constant radiance offset, a THEMIS calibrated radiance spectrum is converted to effective emissivity by finding the highest brightness temperature between bands 3 and 9 (7.9–12.6 μm), and then dividing the radiance spectrum by the Planck function that corresponds to that brightness temperature. This method is similar to that used by *Christensen* [1998] for emissivity determination from Viking IRTM radiance data. Note that surface emissivity is likely not equal to 1 across a full THEMIS bandwidth of ~1 μm and the atmosphere is not transparent in any THEMIS channel, therefore the highest brightness temperature is likely to be an underestimate of surface kinetic temperature [*Bandfield et al.*, 2004b]. Incorrect kinetic temperature calculation may cause slight errors in the derived emissivity shapes (such as a subtle negative slope toward long wavelengths); however, this effect is minor [*Kahle*, 1987], especially over the limited wavelength coverage of THEMIS. The spectral shape relative to the channel set to unity is suitable for compositional interpretation and distinguishing spectral units.

[18] The effective emissivity spectrum contains a surface emission component and also atmospheric absorptions which attenuate the surface radiance [*Bandfield et al.*, 2004b]. To determine the surface emissivity, it is necessary to separate atmospheric dust and ice absorptions from the measured emissivity. The method applied in this work for atmospheric dust and average water ice aerosols removal [*Bandfield et al.*, 2004b] is not automated and requires some user knowledge of the scene. A large, relatively uniform area in a THEMIS image is selected as a training region, and the effective emissivity from each pixel within that region is averaged. TES spectra are selected from this region and are used to produce a "known" surface emissivity spectrum. The TES spectra are averaged and deconvolved with mineral and atmospheric dust, water ice, and synthetic CO_2 and water vapor end-members to produce a surface emissivity spectrum [*Smith et al.*, 2000; *Bandfield*, 2002] (section 2.1.1). The TES surface emissivity is convolved to the THEMIS spectral band passes to produce a known surface spectrum between bands 3 and 9 (7.9–12.6 μm) for the training region. However, known surface emissivity for bands 1 and 2 (6.8 μm) cannot be derived with this technique because the TES atmospheric end-members used in this study (described by *Bandfield et al.* [2000b], *Smith et al.* [2000], and *Bandfield* [2002]) and TES-derived surface emissivity have a limited wave number range from 233–507 cm^{-1} (19.7–42.9 μm) and 825–1301 cm^{-1} (7.7–12.1 μm). To derive the known surface emissivity for bands 1 and 2, water vapor and CO_2 hot band absorptions are removed from the previously selected TES effective emissivity spectra, using the method of *Bandfield and Smith* [2003]. The short wavelength spectral features of the gas-removed spectra are now due almost entirely to surface emissivity; atmospheric dust and water ice have little influence on effective emissivity at wave numbers greater than ~1300 cm^{-1} [*Bandfield and Smith*, 2003]. The gas-removed spectra are averaged and convolved to the THEMIS spectral band passes, and the band 1 and 2 emissivity value is used to complete the final 9-band known surface emissivity spectrum. Finally, the completed training spectrum is divided from the average emissivity of the THEMIS training region to obtain the atmospheric component. The derived atmospheric component for the training region is assumed to be the atmospheric contribution to the entire image, and is divided from each pixel emissivity spectrum to produce a surface emissivity cube. Note that the assumption of constant atmospheric contribution is not valid for images that cross large changes in altitude. In summary, surface emissivity that is known with TES at the $\sim 10^4$ m scale can be used to derive THEMIS surface emissivity at the individual pixel level (10^2 m scale) as long as the region of known surface emissivity within the THEMIS image is located at a similar elevation as the region of interest.

[19] Atmospheric water ice can be variable on small spatial scales, therefore a different technique must be used to correct for variable ice contributions. This work uses the spectral unit mapping method of *Bandfield et al.* [2004b] for ice removal, whereby the TES-derived water ice shape [*Bandfield et al.*, 2000b; *Smith et al.*, 2000] is degraded to THEMIS spectral resolution and input as an end-member into a linear deconvolution algorithm for that image [*Gillespie*, 1992b; *Ramsey*, 2002]. The resultant water ice concentration map is multiplied by the water ice shape to produce the total ice contributions; the contributions are then removed from the surface emissivity cube.

[20] Using the techniques described above, surface emissivities for bands 3–9 (7.9–12.6 μm) can be determined to <0.01 for relatively warm surfaces (>245 K) [*Bandfield et al.*, 2004b]. Band 10 (14.9 μm) is centered within the atmospheric CO_2 fundamental absorption, and is not used for surface sensing. Note that daytime surface temperatures for some portions of Ares Vallis in the images shown here are colder (~239 K) than ideal for obtaining the best signal-to-noise ratio; however, derived relative differences in emissivity between spectral units can be verified by examining TES atmospherically corrected surface emissivity from the areas of interest. Images acquired of the study region during warmer periods do exist and were analyzed using the same methods described above; however, those images are not shown here because they either contain data dropouts or abundant water ice clouds. Derived surface emissivity from these warmer images are consistent with that derived from the images shown here.

[21] In this work, the decorrelation stretch (DCS) technique [*Gillespie et al.*, 1986; *Gillespie*, 1992a] is used to highlight spectral variability within THEMIS radiance and emissivity images. Using the DCS, unique spectral units can be identified by differences in color; variations in intensity of the same color usually indicate differences in temperature or contrast within one spectral unit. Spectra from color units identified in the decorrelation stretched images are extracted and averaged for spectral comparison and compositional interpretation.

2.2.3. Spectral Unit Mapping

[22] Unique spectral units are identified using DCS images. The spectral unit mapping technique of *Bandfield et al.* [2004b] is used to more accurately determine the distribution of these units. In this method, representative spectra are extracted from each spectral unit in the DCS image, and are treated as scene end-members. Additional

end-members include water ice, for water ice removal, and blackbody, to account for variable spectral contrast. These end-members are then used in a linear deconvolution routine similar to that of [*Gillespie*, 1992b; *Ramsey et al.*, 1999] to produce a more quantitative determination of the composition of pixels composed of mixtures of each spectral unit than can be done from DCS analysis alone. The quality of fit to the measured emissivity by the spectral end-members is indicated by the RMS (root-mean-square) error image, where RMS error is calculated for each pixel [*Bandfield et al.*, 2004b].

2.2.4. Thermal Inertia Derived From THEMIS Data

[23] The parameter of thermal inertia can be used to infer the average particle size or degree of induration of a surface, and aid in the interpretation of the origin of unique spectral units. Surface temperatures measured from orbit are controlled primarily by the thermal inertia and albedo of the surface, as well as latitude, solar longitude, time of day, atmospheric pressure, and atmospheric dust opacity [*Kieffer et al.*, 1977; *Jakosky et al.*, 2000; *Mellon et al.*, 2000; *Fergason and Christensen*, 2003]. Thermal modeling can be used to determine the expected temperature of a surface at a given local time, latitude, solar longitude, and elevation, as a function of thermal inertia. For this work, a thermal model developed by H. H. Kieffer was used to derive thermal inertia values for the Ares Vallis region. Model input parameters were selected to be specific to the geographic location of Ares Vallis and the time of data acquisition. Visible dust opacity was set to 0.2, after *Mellon et al.* [2000]. Higher dust opacities would give increased thermal inertia values, but the increase is small ($\sim$25; units of J m^{-2} K^{-1} $s^{-1/2}$ used throughout) for an opacity of 0.5 on a typical surface with a thermal inertia of 300. Dust opacity will have more of an effect on derived thermal inertia for high inertia surfaces. The calculated thermal inertia values varied by 20–80 for lower inertia surfaces and 90–180 for higher inertia surfaces, due to variable dust opacity. Thermal inertia values reported in this study are calculated from at least 3 different nighttime images over the same surface, and the full range of derived values is given.

2.3. Other Data Sets

[24] Other data sets used in this work include MGS Mars Orbiter Laser Altimeter (MOLA) [*Smith et al.*, 2001] data and Mars Orbiter Camera (MOC) [*Malin and Edgett*, 2001] wide-angle and narrow angle images. Altimetry data are extracted from the standard MOLA 128 pixels per degree (ppd) binned elevation map. TES bolometric albedo and surface dust cover index (DCI) [*Ruff and Christensen*, 2002b] are used to distinguish dust-covered areas (DCI $<\sim$0.94) from less dusty areas (DCI $>\sim$0.97). The DCI for a given spectrum is calculated by averaging TES effective emissivity between 1350–1400 cm^{-1} ($\sim$7.1–7.4 μm) [*Ruff and Christensen*, 2002b].

2.4. Data Set Coregistration for Consistent Surface Observations

[25] Coordinates associated with each TES spectrum are referenced to the IAU/IAG 1994 prime meridian, while the THEMIS image coordinates are referenced to IAU/IAG 2000. This change in coordinate system results in a 0.271° longitudinal offset between the TES and THEMIS data sets. In the present work, the longitudinal shift (toward the east) was applied to all TES data. Small registration offsets in map-projected TES albedo, MOC wide-angle mosaics, MOLA topography and THEMIS images were adjusted manually by lining up well-defined morphologic and albedo features. A geographic information system was created in ArcView 8.0 (ESRI) using the above data sets; this allowed for simple geologic mapping of units, defined by their thermophysical, compositional, and geomorphic characteristics, within an accurate three-dimensional context. Topographic profiles over areas of interest within a THEMIS image, derived from the 128 ppd binned MOLA elevation data, were selected using JMARS data analysis software [*Gorelick et al.*, 2003].

3. Results

3.1. Spectral Units

[26] THEMIS daytime infrared images within the study region ($\sim$338–342.5°E, 3–8°N) were selected for spectral analysis. All wavelength bands of the selected images were mosaicked together, and a decorrelation stretch [*Gillespie et al.*, 1986; *Gillespie*, 1992a] was applied to the normalized radiance mosaic using bands 5, 7, and 8 projected as red, green, and blue respectively (Figure 1). The 5-7-8 combination was initially chosen in an effort to distinguish TES Type 1 and 2 surfaces [*Bandfield et al.*, 2000a], if present; other band combinations were also evaluated and found to display approximately the same degree of spectral variability in the study region. Only a portion of the study region is shown in Figure 1, in order that details of the channel floor may be resolved. Relative to many low-albedo regions on Mars, the Ares Vallis region displays a high degree of spectral variability at THEMIS resolution. Three primary spectral units are readily apparent in the DCS images: a royal blue unit, a magenta unit, and a green unit. The west-to-east color variations from red to purple within the magenta unit (Figure 1) are an artifact of the normalization/mosaicking process. Three individual images that contain the blue, magenta and green color units were chosen for detailed spectral analysis (Figure 2). Note that these spectral units are throughout referred to by the color they appear as in the DCS mosaic using bands 5, 7, and 8.

[27] Average THEMIS emissivity spectra from magenta, blue, and green color units are shown in Figure 3. Each spectrum is the average of at least 90 pixels. The surface emissivity spectra are compared with the TES Type 1 and 2 spectra derived by *Bandfield et al.* [2000a], and the olivine-rich surface spectrum from Nili Fossae [*Hoefen et al.*, 2003] convolved to the THEMIS spectral band passes. Despite uncertainties in the atmospheric removal techniques, the relative differences in surface emissivity between each color unit remain constant in the three different images (Figure 3). Blue areas have emissivity shapes that are similar to Type 1 materials between bands 3–9 (7.9–12.6 μm), with the primary absorption located at band 5 (9.4 μm) and a concave-upward shape between bands 6–8 (10.2–11.8 μm). Magenta areas in the decorrelation stretch mosaic have a relatively lower emissivity at band 7 (11.0 μm) and higher emissivity at band 5 (9.4 μm), compared to blue areas and to TES Type 1. Green area emissivity shapes have a primary absorption at band 5 (9.4 μm), similar to blue

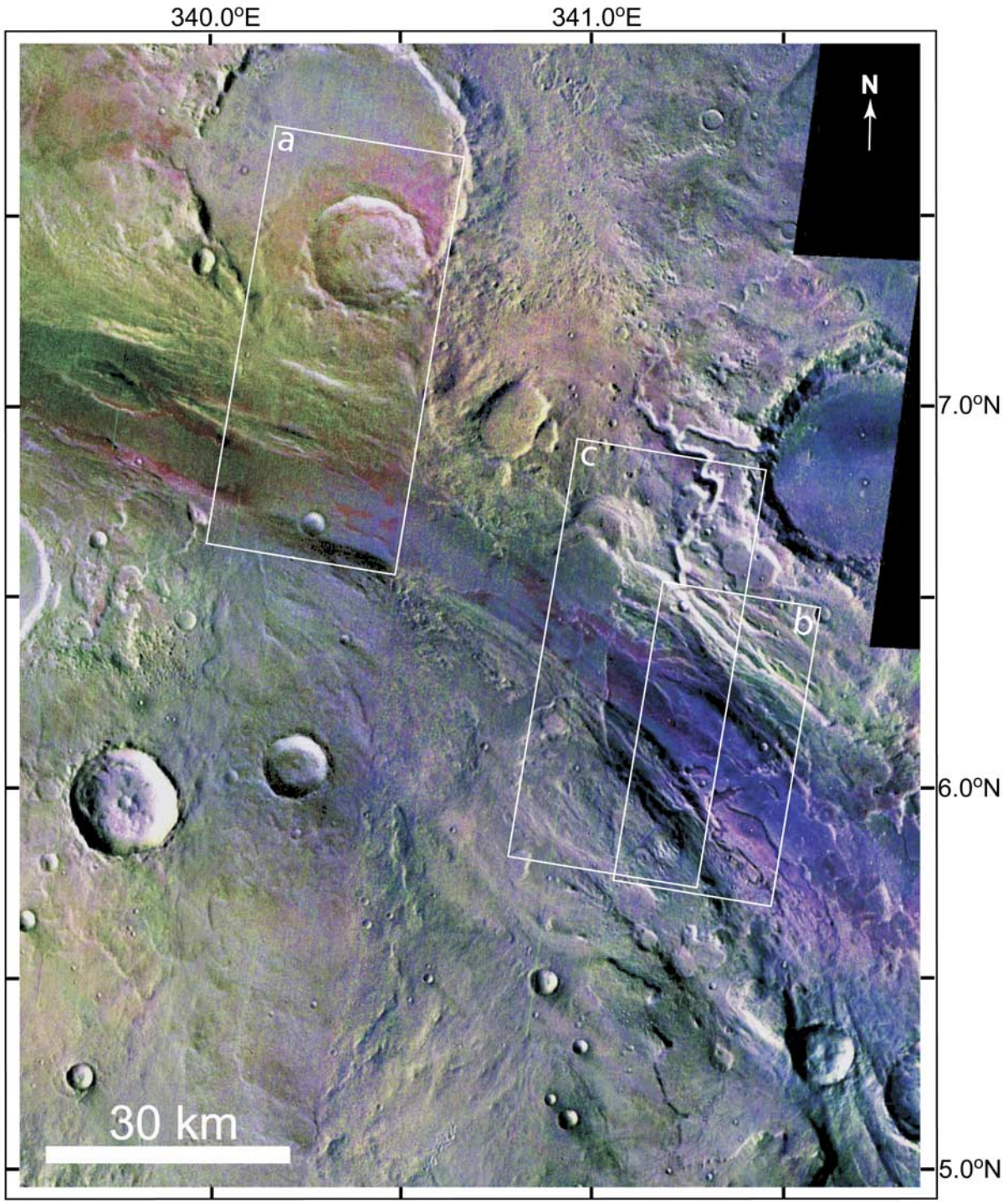

Figure 1. Mosaic of THEMIS daytime radiance images, with a decorrelation stretch applied using bands 5, 7, and 8 represented as red, green, and blue, respectively. Bounding coordinates are 339.5–341.9°E, 4.95–7.95°N; the area shown represents the majority of the study region (see text). Primary spectral units found in the Ares Vallis region are represented as blue, magenta, and green colors. White boxes indicate areas that are shown in Figure 2.

areas, but also have a concave-downward shape between bands 6–8 (10.2–11.8 μm) and a steeper slope between bands 6–7 (10.2–11.0 μm). Note that the band 1 and 2 (6.8 μm) relative emissivity values are highly variable between the 3 images and are also greater than unity for 2 of the images. Cold surface temperatures (~238–245 K for the coldest surfaces) are the likely cause for the observed band 1 and 2 variability (see section 2.2.2).

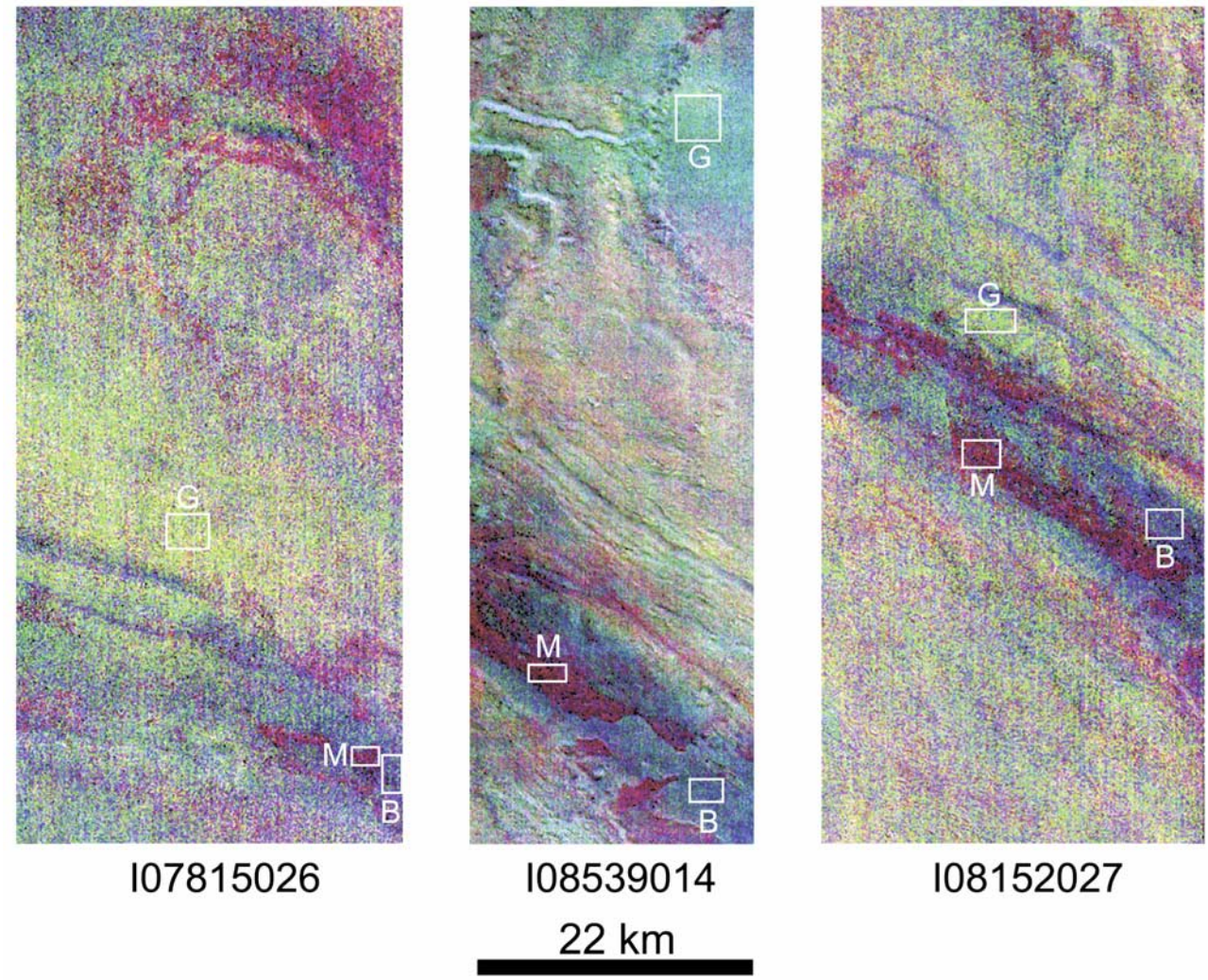

Figure 2. Three examples of areas that were selected for spectral analysis with THEMIS. The images shown are atmospherically corrected surface emissivity cubes, which have been processed using a decorrelation stretch of bands 5, 7, and 8. The white boxes represent regions that spectra were extracted from and averaged for surface emissivity comparison. At least 90 pixels were used in each average. For each panel, spectra were selected from blue, magenta, and green units and are displayed in Figure 3. From left to right the images are I07815026, I08539014, and I08152027.

[28] Within the spectral region of the Si-O fundamental absorption (~9–12 μm), the shift to longer wavelengths of the major emissivity minimum from DCS green and blue surfaces to DCS magenta surfaces indicates a greater abundance of mafic minerals, such as pyroxene and olivine [e.g., *Lyon*, 1965], in the magenta unit than in the green and blue units. The difference in band 7 (11.0 μm) emissivity between the green and blue units suggests a greater abundance of high-silica materials in the green unit relative to the blue unit.

[29] Representative THEMIS surface emissivity spectra from each color unit were input as scene end-members into a linear deconvolution model for three image surface emissivity cubes with water ice concentration removed [*Bandfield et al.*, 2004b]. A blackbody end-member was included to account for variable spectral contrast within the scene, and the spectral fitting was constrained to THEMIS bands 3–9 (7.9–12.6 μm). An example of the model results for one image is shown in Figure 4. Inspection of the RMS error image shows that all areas are well-modeled by 1 or more of these color units, with the exception of areas that are shadowed by topography, indicating that the scene is accurately described by these three units. Errors in the shadowed areas are likely due to colder surface temperatures (resulting in lower signal-to-noise). In the example shown, shadowed areas are 3–8 K colder than the coldest nonshadowed areas. Spatially coherent variations in modeled end-member concentrations give additional confidence that these end-members represent the range of surface spectral units in this area.

3.2. Thermophysics and Surface Properties of Spectral Units

[30] Figures 5a and 5b show a pair of daytime and nighttime THEMIS mosaics of the upper Ares Vallis region. Thermophysically distinct units are exposed in the floor and walls of Ares Vallis, as well as in the surrounding craters and plains. Figure 6 highlights characteristic thermophysical

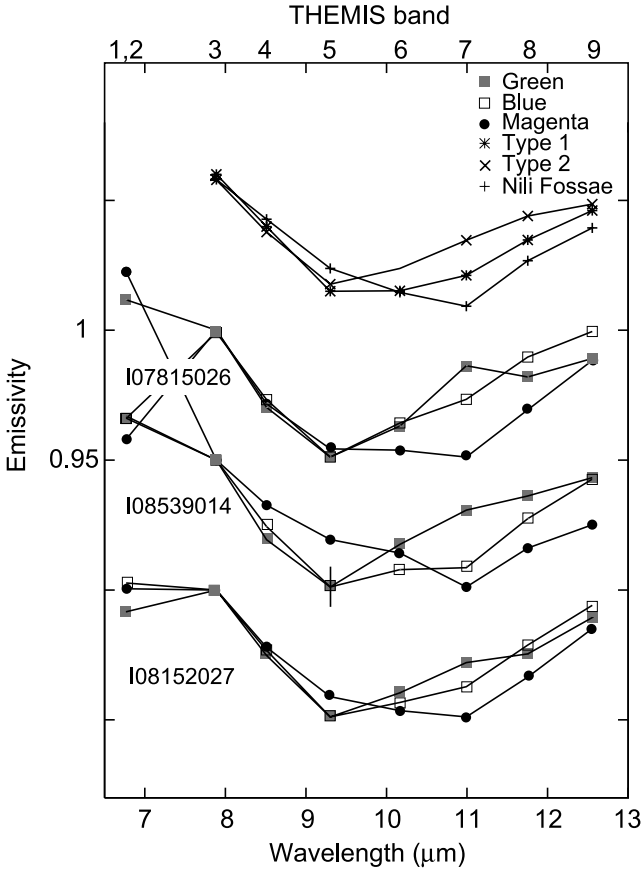

Figure 3. Average surface emissivity spectra of magenta (solid circle), blue (open square), and green (solid square) color units from the three images shown in Figure 2. Spectra are compared with the TES Type 1 and Type 2 end-member spectra from *Bandfield et al.* [2000a] and the Nili Fossae olivine-rich surface spectrum [*Hoefen et al.*, 2003] convolved to the THEMIS spectral band passes. Spectra are offset for clarity and are contrast-adjusted to emphasize differences in the spectral shape of each color unit. The typical $\pm\sigma$ variance for bands 3–9 of each average spectrum is represented by the vertical line in the center of the plot. Note that relative spectral differences between the three color units are constant for each image, despite uncertainties in atmospheric correction.

variations found within each spectral unit, while Figure 7 shows geomorphologic and relative brightness variations within each spectral unit.

3.2.1. DCS Blue

[31] Blue surfaces are typically associated with the lowest albedo areas. This unit occurs primarily in the channel floor and is darker than higher-standing plateaus and mesas found near the channel floor (Figure 7). TES bolometric albedo of the blue unit ranges from 0.11–0.14, and DCI values range from 0.967 to 0.981. These values are consistent with the presence of a sand component with little dust cover. THEMIS-derived thermal inertia (TI) values from 2 different areas (Figures 6 and 7, areas A and B) within the blue unit range from 570 to 725. Although these TI values are greater than that of dune-forming sand (~350 [*Edgett and Christensen*, 1991]), the high TI could be explained by a mixture of sand and coarser (mm to cm) particles or a lower thermal inertia layer (sand) overlying a high thermal inertia layer (rock). The blue spectral unit is interpreted as a layer of loose sand and gravel overlying rock.

3.2.2. DCS Magenta

[32] Magenta surfaces are typically associated with the highest thermal inertia materials in the Ares Vallis region (670–840, Figures 6 and 7, area C), and is characteristically a cliff-forming unit, with plateaus and mesas that stand 10–250 meters above the surrounding floor materials (Figure 7). In some areas these mesas appear relatively brighter than their surroundings in MOC and THEMIS visible images (Figure 8); however, TES albedo of these areas ranges from 0.12 to 0.14. The slightly increased brightness is likely due to a thin veneer of bright dust and/or less dark sand on these highstanding areas compared to the surrounding floor. The magenta unit typically has either a pitted or scoured appearance, although in some areas it appears smooth at the resolution of the THEMIS visible imagery. Finally, a few areas within the magenta unit exhibit TI values between 320–410; these areas are not associated with mesa or plateau landforms.

3.2.3. DCS Green

[33] Green surfaces are typically associated with intermediate thermal inertia units in layered wall materials found near the channel floor (415–500, Figures 6 and 7, areas D and E) but is also associated with some of the lowest thermal inertia materials on the plains (290–380, areas F and G). DCI values range from ~0.957 to ~0.981, and TES albedo ranges from 0.13 to 0.15.

3.3. Mineralogy

[34] In an effort to better constrain the mineralogy of the primary surface components, TES spectra were extracted from the largest of these areas. The THEMIS magenta, blue, and green areas are large enough to obtain multiple TES spectra for averaging and deconvolution analysis, although in some areas TES data is limited. Figure 9 shows atmospherically corrected surface spectra from each color unit. The green unit is extensive enough that >170 spectra were available for averaging. For this unit, surface emissivity was derived by averaging 13 to 36 spectra from seven different orbits, and the spectrum shown is the average of the derived surface emissivity from each orbit. This method was not possible for the magenta and blue units because only 1–2 orbits covered these regions. However, these orbits were part of the seven orbits used to derive the green unit surface emissivity, and the consistency in the derived green unit surface emissivity shape from all 7 orbits gives confidence in the accuracy of the magenta and blue unit surface emissivity shapes.

[35] An example of the modeled contribution of each mineral group to the derived surface emissivity is given for the DCS green unit in Figure 10. The average spectrum of each unit was deconvolved in a similar manner to give the derived mineral concentrations [*Ramsey and Christensen*, 1998; *Bandfield*, 2002]. These values were converted to chemical oxide weight percentages [*Hamilton and Christensen*, 2000; *Wyatt et al.*, 2001; *McSween et al.*, 2003]. The results for each unit are given in Table 2.

3.3.1. DCS Blue

[36] Four TES spectra with similar atmospheric conditions were found that isolate the DCS blue unit. The major

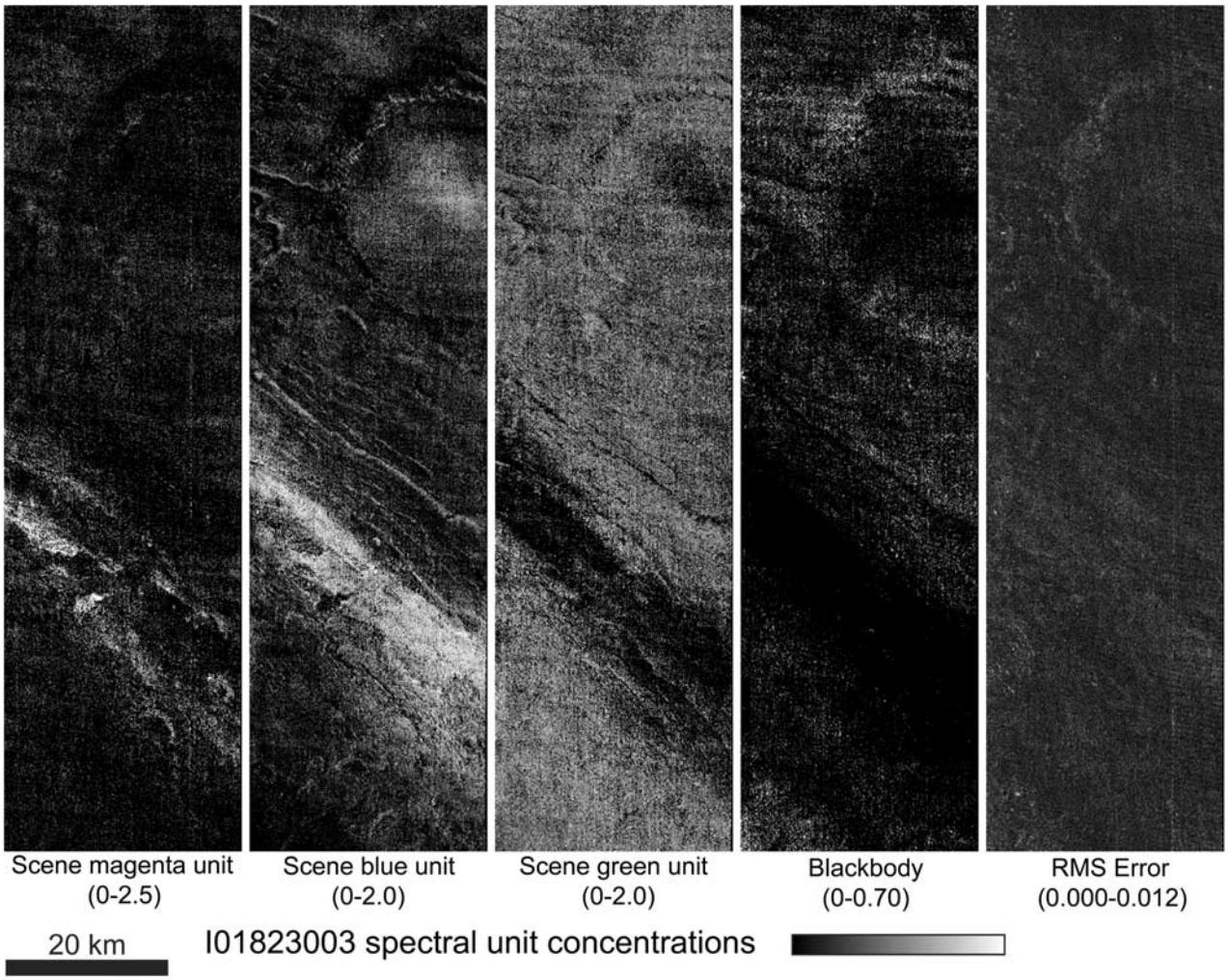

Figure 4. Spectral unit concentration maps for a portion of THEMIS image I01823003. The center coordinates of the portion of the image shown are 341.5°E, 6.4°N. Inspection of the RMS error map indicates that all areas are well-modeled by the input end-members: scene magenta unit, scene blue unit, scene green unit, and blackbody. No other components are needed to model the surface emissivity of this region.

mineral components of the DCS blue surface are feldspar (30%), pyroxene (25%–80% of which is clinopyroxene, 20% is orthopyroxene), and high-silica materials (25%) (Table 2). Sulfates, carbonates and olivine are included in the model fit at concentrations of <15%. Spectral shape comparison of the surface spectrum with TES Type 1 and Type 2 shapes [*Bandfield et al.*, 2000a] indicates that the DCS blue surface is similar to Type 1 between 233–507 cm^{-1}; however, there is a slight shift in the position of the primary absorption between 800–1300 cm^{-1} to higher wave numbers (Figure 9).

3.3.2. DCS Magenta

[37] Eight TES spectra of similar atmospheric conditions were found to cover magenta surfaces. Deconvolution of the average magenta unit spectrum gives primarily pyroxene and olivine (Table 2). However, analysis of THEMIS visible images and TES albedo shows that the majority of the aerial extent of the magenta unit where TES spectra were extracted is covered by some thickness of the sand layer (inferred by relative darkness variations across the unit). The sand layer, which is spectrally different than the magenta mesa-forming unit (section 3.3.1), is contributing to the deconvolved mineralogy of the DCS magenta unit. To isolate the magenta unit from the sand unit (DCS blue), the average surface emissivity spectrum from the blue unit was subtracted from the average surface emissivity of the magenta surfaces (see also *Ruff et al.* [2001] for a description of this technique). The concentration of blue unit emissivity to be subtracted (~50%) was determined by examining the area within THEMIS visible images where the magenta-surface TES spectra were extracted and estimating the percentage of sand coverage within that area. The isolated magenta unit surface spectrum was then computed using

$$\varepsilon_{\text{isolated magenta surface}} = \left(\varepsilon_{\text{magenta\&blue surface}} - \varepsilon_{\text{blue surface}} * 0.50\right)/0.50 \quad (1)$$

and is shown in Figure 11a. Note that equation (1) could give values greater than 1.0 if the spectral contrast of the DCS blue surface were greater than that of the DCS

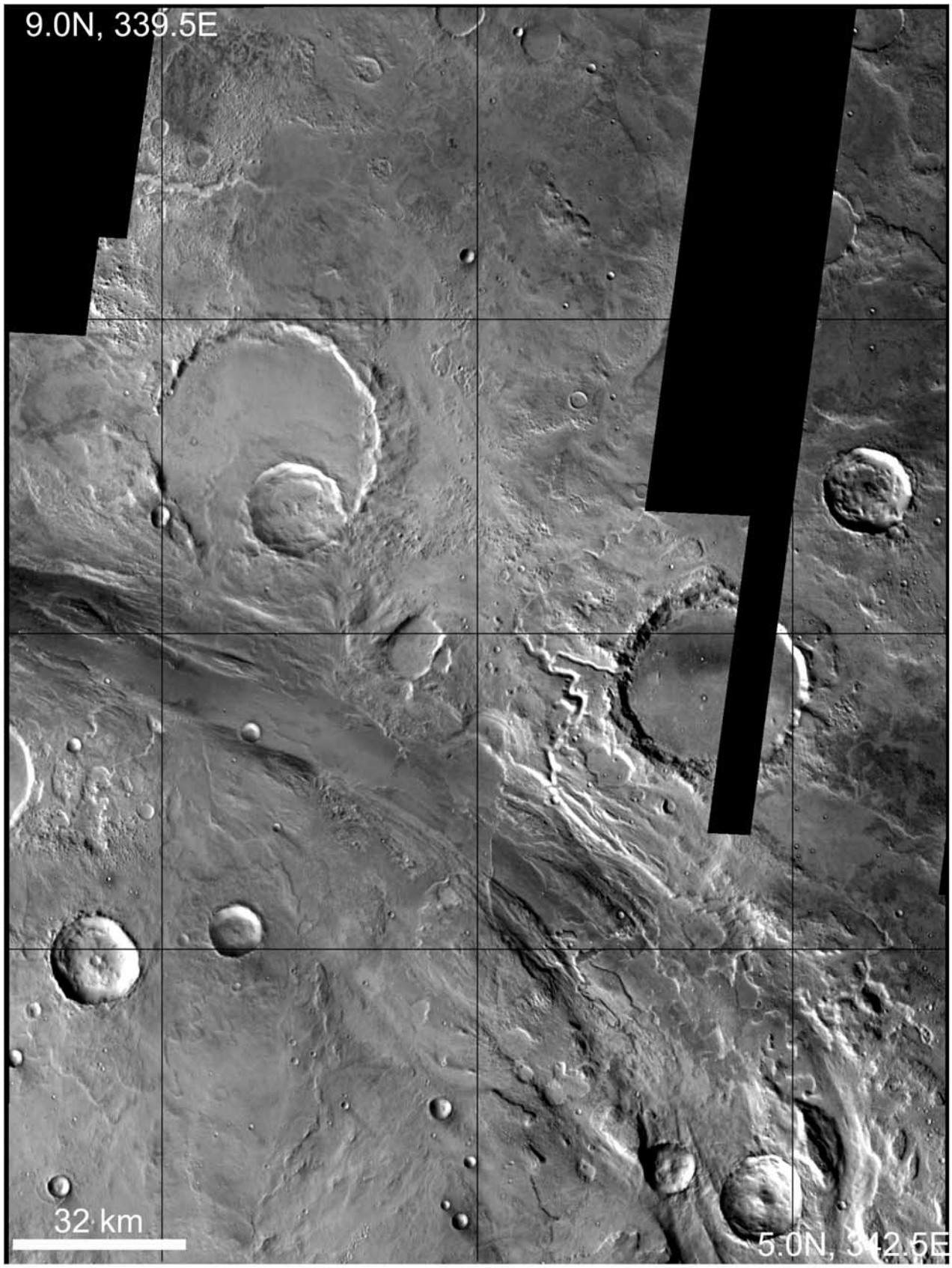

Figure 5a. THEMIS daytime band 9 radiance mosaic. Images are normalized to the highest radiance within the mosaic to remove orbit-variable effects such as season, time of day, and atmospheric dust opacity. Darker tones indicate cooler temperatures.

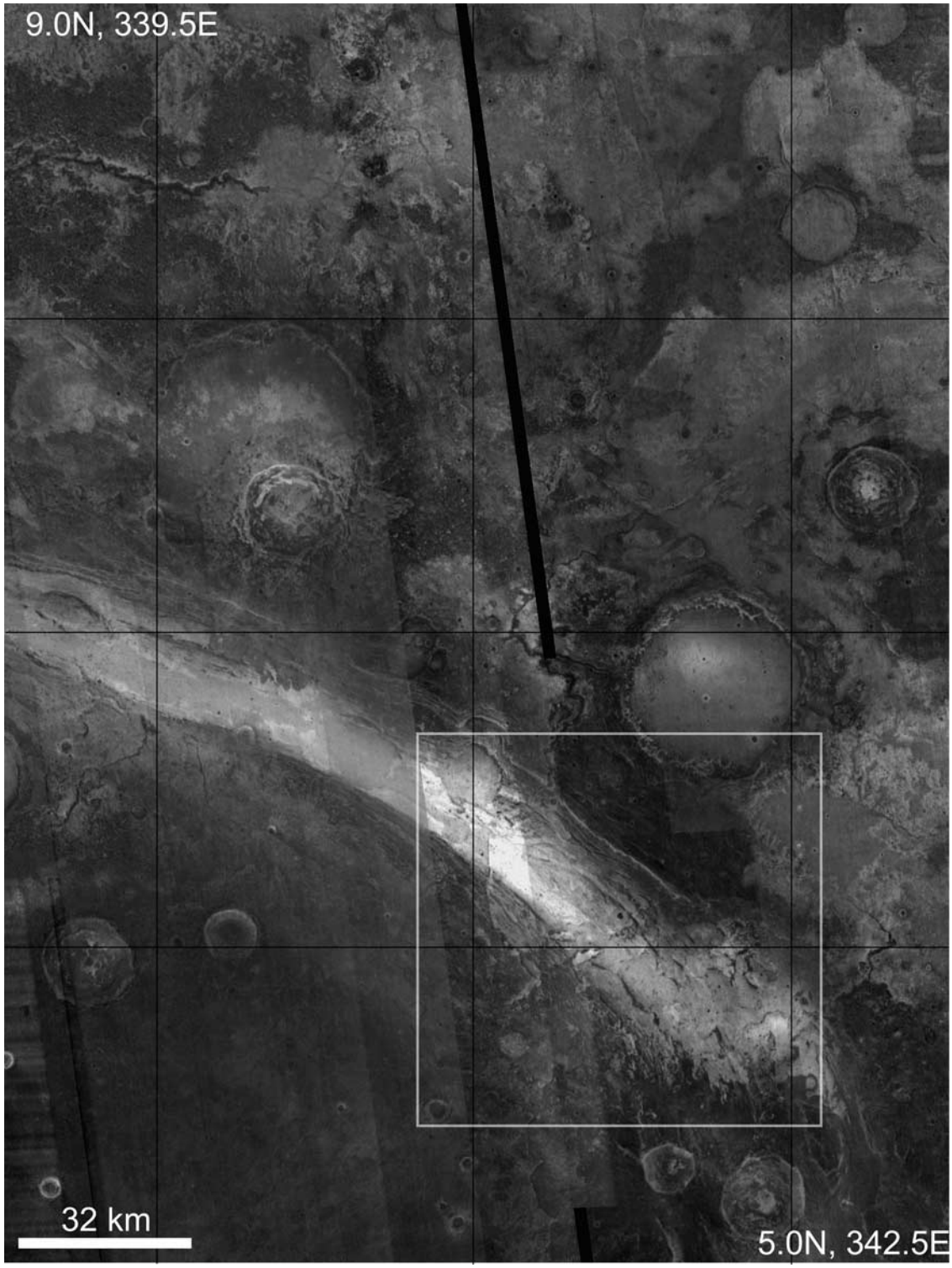

Figure 5b. THEMIS nighttime band 9 radiance mosaic. Images are normalized to the highest radiance within the mosaic to remove orbit-variable effects such as season, time of day, and atmospheric dust opacity. Light tones indicate higher temperatures. The warmest materials at night are located on the channel floor. These surfaces have relatively cooler temperatures during the day, which is characteristic of rocky material. The white box indicates the area shown in Figure 6.

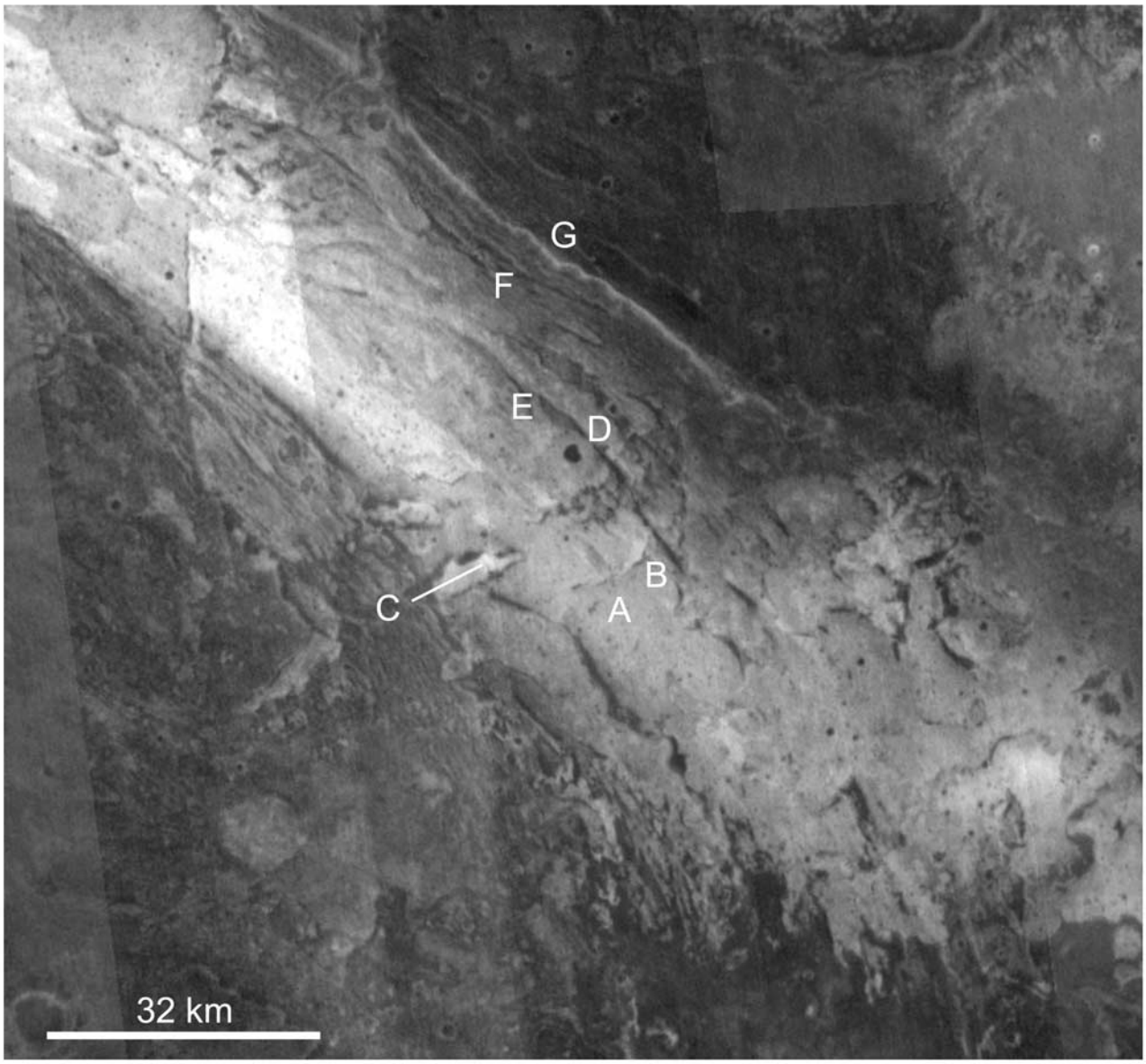

Figure 6. A portion of the nighttime radiance mosaic shown in Figure 5b. Letters designate areas within each spectral unit where thermal inertia values were derived. Units are J m^{-2} K^{-1} $s^{-1/2}$. A, DCS blue unit, 625–725; B, DCS blue unit, 570–650; C, DCS red unit, 670–840; D, DCS green unit, 435–500; E, DCS green unit, 415–450; F, DCS green unit, 350–380; G, DCS green unit, 290–308.

magenta plus blue surface; however, that is not the case in this region. The isolated magenta surface spectrum was then deconvolved with the spectral end-members from Table 1, excluding mineral groups that were not used in model fits of the original magenta unit spectrum. New model fits yield modal pyroxene (45%, greater than 90% of which is clinopyroxene) and olivine (25%) as the major components (Figure 11a, Table 2). Note that the strong absorption feature at 900 cm^{-1} (11.1 μm) is diagnostic of olivine.

[38] To verify that the magenta surface spectrum is well-isolated, this spectrum was convolved to the THEMIS spectral band passes and compared with the average surface emissivity from an area within the magenta unit in THEMIS image I08539014 (Figure 11b). The selected area for comparison is ~10 km upstream from the area where the TES emissivity spectra were extracted, and has a strong magenta unit concentration in the results from spectral unit mapping (section 3.1). The overall similarity between these shapes ($\Delta\varepsilon < 0.01$) indicates that the derived sand-free TES surface emissivity of the magenta unit is well isolated.

[39] To better constrain the composition of the olivine component found in Ares Vallis DCS magenta surfaces, a ratio spectrum was created using single-orbit TES spectra from a blue surface and a magenta surface (Figures 12a and 12b). The major absorption positions in the ratio spectrum (Figure 12c) match well with an olivine composition of Fo_{60}. Differences between the ratio spectrum and the olivine spectrum are present because a ratio spectrum

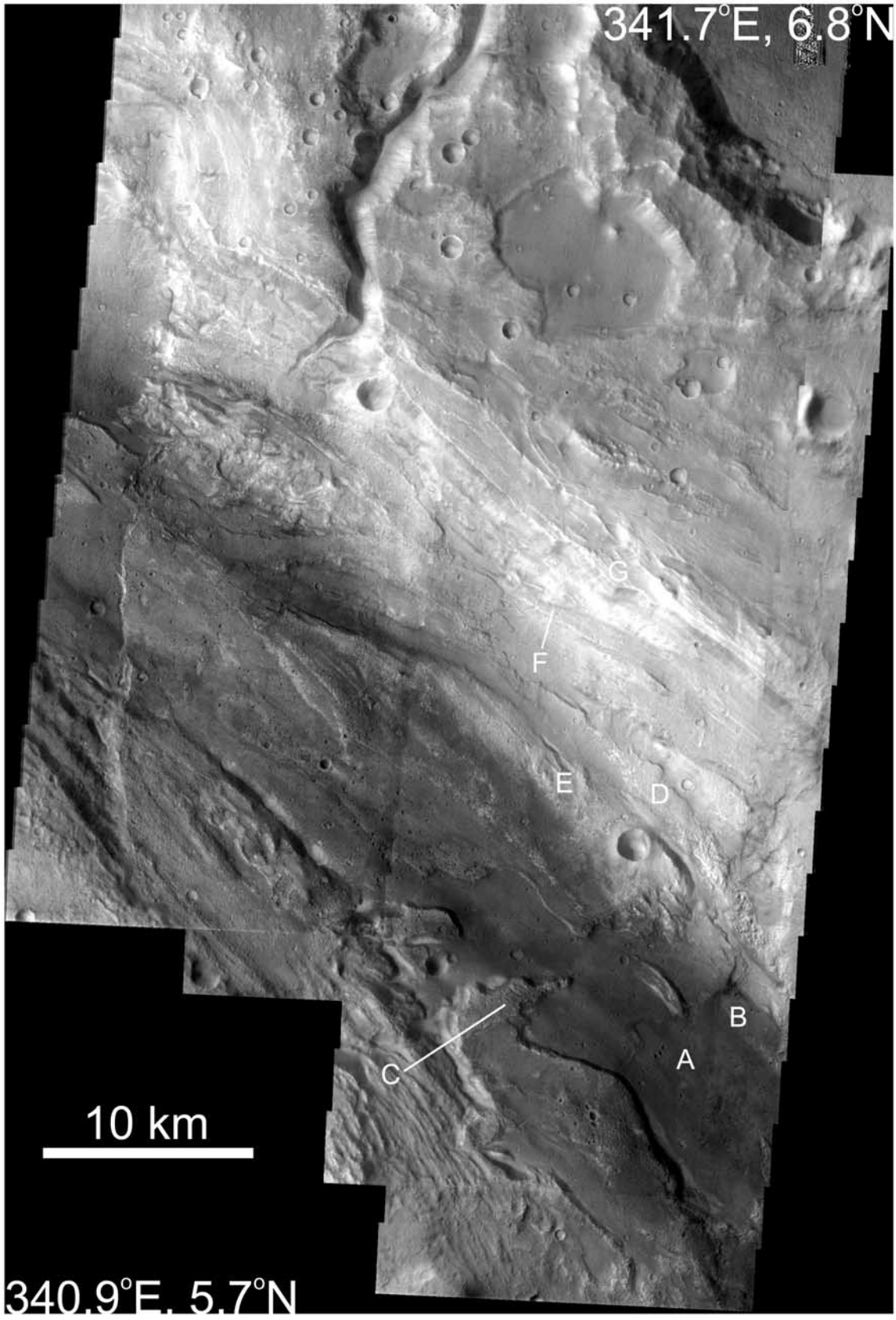

Figure 7. THEMIS visible image mosaic of the center portion of Figure 6. Letters correspond with thermophysical units designated in Figure 6. Relative brightness differences occur throughout the area. TES albedo of the darkest areas is ~0.11, consistent with coarse-grained particulates. Small mesas that are relatively brighter than the sand can be distinguished (see high-resolution example in Figure 8).

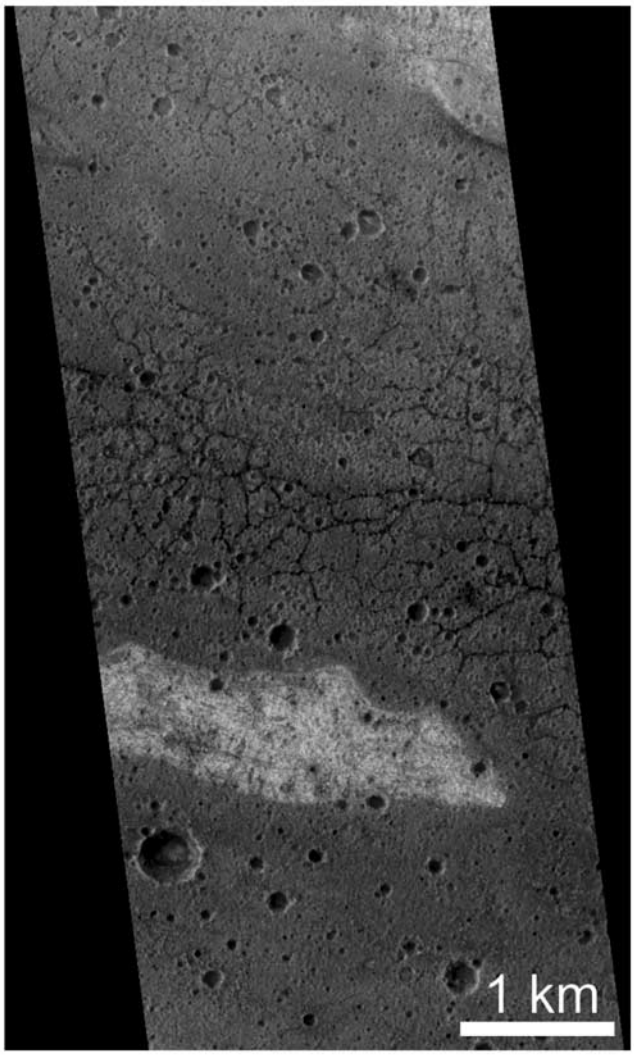

Figure 8. A portion of MOC image R0200625. Pixel width is 6.14 m. The area shown is located near the lower right corner of box a in Figure 1, at ~340.4°E, 6.7°N. The light-toned surface is part of the magenta unit. The dark-toned surface is part of the blue unit. Small dendritic to polygonal forms (~20 m wide) that may be cracks are found in the floor materials. The image is courtesy of NASA/JPL/Malin Space Science Systems.

contains residual features from both surfaces used in the ratio and also because the isolated magenta unit is not composed purely of olivine (Table 2).

3.3.3. DCS Green

[40] TES effective emissivity spectra from the green spectral unit were extracted from seven different orbits, grouped by orbit and averaged, and then deconvolved to produce seven surface emissivity spectra. The normalized average and standard deviation of these spectral shapes is shown in Figure 9. The modeled fits of this average spectrum indicate that the green unit is dominated by feldspar (20%), pyroxene (15%–80% of which is clinopyroxene, 20% is orthopyroxene), and high-silica components (35%) (Table 2, Figure 10). The average surface emissivity spectrum is similar to TES Type 1 [*Bandfield et al.*, 2000a] at lower wave numbers (Figure 9); however, the shape between 800–1300 cm^{-1} is significantly different than both global end-members. The width of the major absorption at ~1070 cm^{-1} is wider and there is a concave-downward shape between 875–1020 cm^{-1}. This spectral shape is found consistently within the green color unit throughout the Ares Vallis channel walls and surrounding plains.

4. Discussion

4.1. Nature and Origin of Geologic Units

[41] Compositional, thermophysical, and morphological observations are synthesized in an effort to determine the nature and origin of observed spectral units. A geologic sketch map (Figures 13 and 14) of the region was constructed using the spectral unit maps (Figure 4, section 3.1), THEMIS nighttime images, TES bolometric albedo, and THEMIS visible images. Figure 15 is a generalized interpreted stratigraphy of the study region, based on several cross sections using the geologic sketch map (Figure 13) and MOLA data. For reference, a representative transect line for Figure 15 is shown on Figure 13. The tilt of layers shown in Figure 15 may not be representative of actual layer

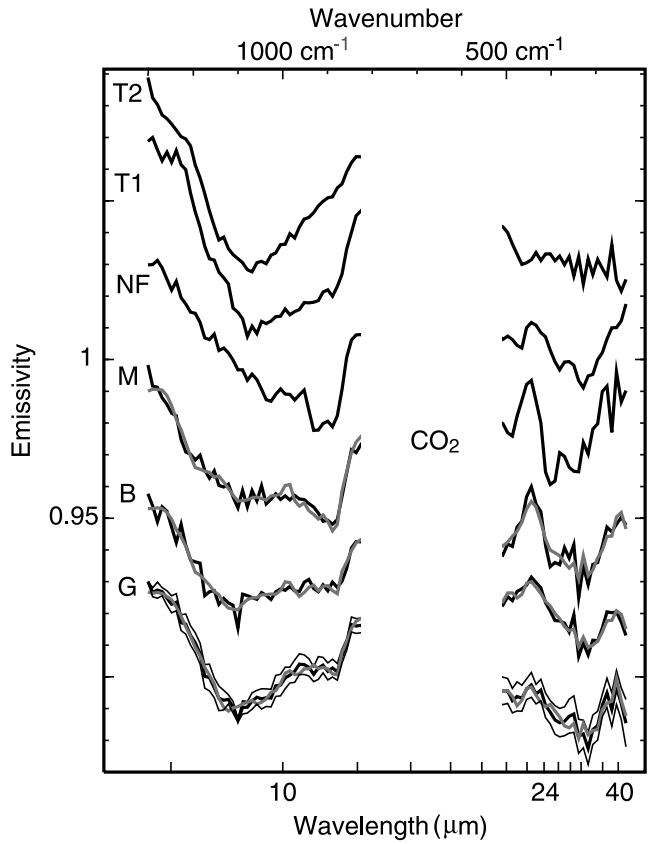

Figure 9. Derived surface emissivity and modeled surface for each color unit (M, magenta; B, blue; G, green). The spectra are compared with Surface Types 1 and 2 (T1,T2) [*Bandfield et al.*, 2000a] and Nili Fossae (NF) [*Hoefen et al.*, 2003]. The DCS green unit surface emissivity is the average of green unit surface emissivity derived from seven different orbits. The ±σ variance is plotted in thin black. See text for explanation. Modal mineral abundances are given in Table 2. All spectra are offset for clarity.

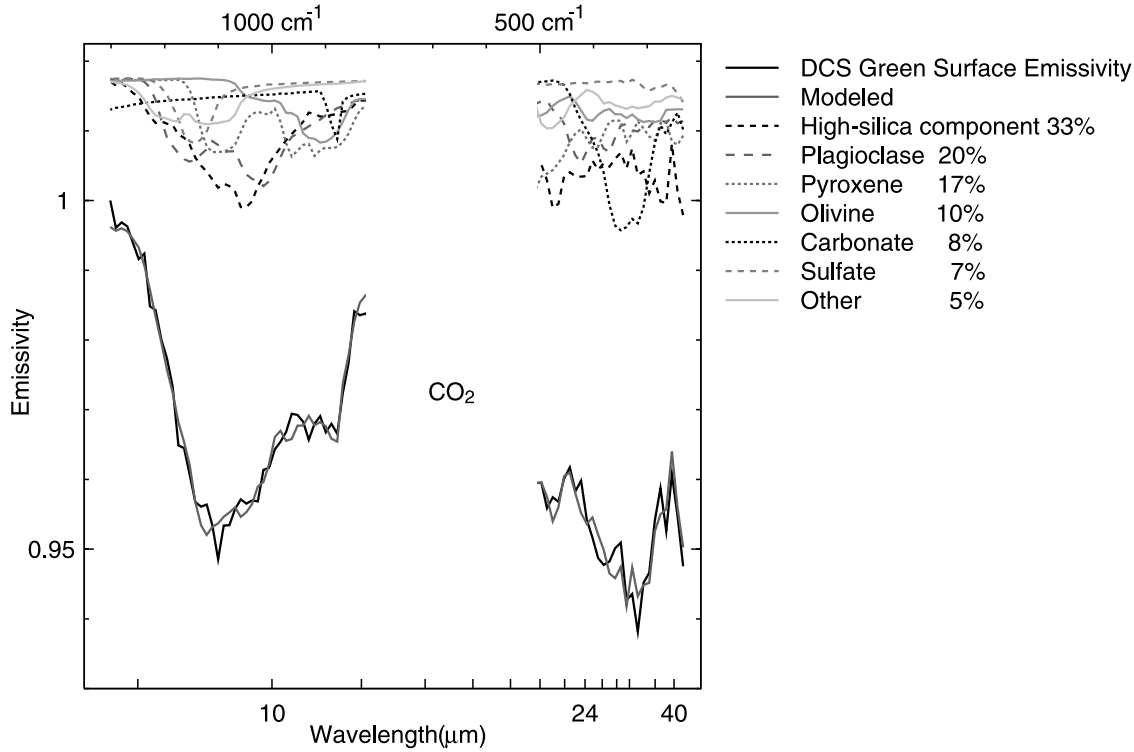

Figure 10. Example of the spectral contribution of each mineral group to the TES-derived surface emissivity for the DCS green unit.

geometry because the regional strike and dip and potential offset of the layers by faulting is unknown; however, in areas where the contact between the magenta and green units are exposed on opposite sides of a mesa, the contact does appear relatively flat (<~0.5% gradient) at the limit of registration accuracy between THEMIS infrared images and binned MOLA data. The distribution and relative stratigraphic position of units in Ares Vallis provide clues to the timing of events and possible environments that may have existed in this area.

4.1.1. Regional Rock Unit (DCS Green)

[42] The green unit is enriched in high-silica component(s) (Table 2, Figure 10). The derived mineralogy and chemistry is consistent with basaltic andesite to andesite, if the high-silica component is due to primary volcanic glass. However, the mineralogy is also consistent with a mixture of basalt and a secondary high-silica component.

[43] The green spectral unit is associated with plains materials and with rock layers that overlie the channel floor magenta unit. The thermal inertia associated with this green spectral unit is variable. Near the channel floor, the green unit thermal inertia is ~415–550 (areas D and E, Figure 6). On the plains, the thermal inertia is as low as 290–380 (areas F and G, Figure 6). The differences are likely due to enhanced aeolian activity within the channel; channel floor materials are probably less dust-covered. DCI values of 0.957–0.970 for the lower thermal inertia areas versus 0.967–0.981 for the green areas on the channel floor, as well as a decreased spectral contrast for the lower thermal inertia green areas support this suggestion. Although the derived thermal inertia values for the green spectral unit are lower than that of magenta surfaces, this unit is also considered to be in-place rock, due to sharp contacts with the magenta unit, association with layered wall rock, and no correlation with the darkest (and presumably mobile) materials.

[44] TES-derived surface emissivity spectra from the green spectral unit consistently exhibit the shape shown in Figure 9. For simplicity, the green unit is hereafter referred to as the "regional rock unit" due to the constant spectral shape in TES data throughout the study area and ambiguity of the primary versus secondary nature of the high-silica component(s) that dominate the modal mineralogy (section 2.1.1).

4.1.2. Olivine-Rich Unit (DCS Magenta)

[45] The magenta unit is enriched in clinopyroxene and olivine (Fo_{60}). The relatively high percentage of olivine and pyroxene and lack of plagioclase in the derived mineralogy of the magenta surfaces might suggest that this unit should be classified as ultramafic [e.g., *Streckheisen*, 1974; *Hess*, 1989, p. 310]; however, the derived 48 ± 2 wt% SiO_2 is 3% higher than the upper limit for terrestrial ultramafic rocks (45%) [e.g., *Le Bas et al.*, 1986]. Given the uncertainties that arise from averaging only 8 emissivity spectra and from the magenta unit isolation process, this rock is hereafter referred to as the olivine-rich unit, and we refrain from assigning a particular lithologic name. Note that the low derived Al_2O_3 and high FeO* (total iron) oxide abundances are a similar characteristic to that of the Martian meteorites, and the total derived chemistry most closely matches the chemistry of the picritic shergottite Dar al Gani 489 [*Folco et al.*, 2000]. However, the combined modal mineralogy and

Table 2. Modal Mineralogy and Derived Oxide Abundance for Ares Vallis Spectral Units[a]

Mineral Group/Oxide	Blue	Magenta	Corrected Magenta	Green
Deconvolved Mineralogy,[b] %				
Feldspar	30	(10)	(5)	20
Pyroxene	25	40	45	15
High-silica (Si/O >0.35) component	25	(10)	(0)	35
Olivine	(5)	15	25	(10)
Hematite	(0)	(0)	(0)	(0)
Carbonate	(10)	(10)	(10)	(10)
Sulfate	(10)	(5)	(5)	(5)
Other	(0)	(5)	(10)	(5)
Blackbody	70	55	70	65
RMS error, %	0.221	0.276	0.231	0.160
Derived Oxide Abundance,[c] *wt.%*				
SiO_2 (±1.5)	53	50	48	57
Al_2O_3 (±1.7)	15	6	3	13
FeO* (±1.2)	6	14	18	10
MgO (±2.4)	10	17	19	9
CaO (±0.8)	10	10	11	6
Na_2O (±0.4)	1	1	1	2
K_2O (±0.4)	3	1	0	4
TiO_2 (±0.9)	0	0	0	0

[a]Spectral units are referred to by the color they appear in the DCS mosaic (Figure 1).

[b]Plagioclase is the dominant feldspar; augite is the dominant pyroxene. Concentrations are normalized for blackbody and rounded to the nearest 5%. Parentheses indicate concentrations at or below TES detection limits for normalized mineral abundances [*Christensen et al.*, 2000b].

[c]Reported values are normalized for H_2O and CO_2 abundance (refer to *Wyatt et al.* [2001] and *McSween et al.* [2003]) and rounded to the nearest 1%. FeO* designates total iron. Uncertainties shown are the standard deviation of the absolute differences between the measured and modeled bulk oxide values reported by *Hamilton et al.* [2001] for laboratory emission spectra of a suite of terrestrial volcanic rocks, degraded to TES spectral sampling (10 cm^{-1}). Uncertainties are likely to be higher for orbital data.

oxide abundances do not precisely match any of the meteorite samples [e.g., *Banin et al.*, 1992; *McSween*, 1994].

[46] *Hamilton and Christensen* [2004] examined the largest global occurrences of olivine-bearing terrains and show that the strength of the olivine spectral depth is commonly correlated with increased nighttime brightness temperature. Similar to their global results, the olivine-rich units in the Ares Vallis region are also correlated with the highest thermal inertia material in the channel floor and in areas outside of the channel. On the channel floor, the olivine-rich landforms are primarily characterized by high-standing mesas and plateaus. The derived thermal inertia values (575 to 840) and association with erosion-resistant landforms are consistent with the channel floor olivine-rich unit being disaggregated, in-place rock, rather than materials that are transportable by saltation or creep. On the plains, the thermal inertia of most olivine-rich surfaces ranges from 500–550. While these values are lower than those derived for channel-floor materials, these surfaces are still the highest inertia materials found on the plains (Figure 14). This, along with the well-defined boundaries of these surfaces, also supports an association with a disaggregated in-place rock unit. Finally, although the majority of olivine-rich surfaces are associated with rock, there are a few regions with an elevated olivine signature in the surrounding plains that have relatively lower thermal inertia (~320–410) and are likely to be windblown sand-sized particles derived from the in-place olivine-rich units (Figure 13).

[47] The olivine-rich rock unit occurs as two layers in the upper Ares Vallis region, separated by a 1000–1400 m thick section of the regional rock unit (Figure 15). The lower layer is at least 250 m thick in some areas, and outcrops on both sides of the channel floor for a distance of >380 km. It is the lowest exposed unit that is not obscured by sand. Spectrally unmistakable exposures of this lower layer start upstream near the mouth of Aram Chaos at ~342.2°E, 3.1°N and stretch discontinuously northwestward along the channel floor at least to ~338.4°E, 7.7°N, where increasing dust cover begins to obscure the spectral character of surface units (both the westernmost and easternmost of these outcrops are not shown in Figures 1 and 13; see section 3.1).

[48] The second olivine-rich rock layer is exposed in a few topographic lows within the plains (Figures 13–15), and it is at least 100 m thick in some areas. These isolated occurrences of the second layer are found within or adjacent to large impact craters (25–45 km in diameter), located at 341.7°E, 6.8°N, 340.3°E, 7.6°N and 339.4°E, 6.6°N. Two of the areas are found on crater floors, in small outcrops adjacent to the crater wall. The other three occurrences are found nearby these large craters, exposed on the floor of topographic lows (Figure 13) within the plains.

[49] Finally, olivine-rich materials are also found in a ~250 m-thick exposure in the wall of an unnamed 20 km-diameter crater located at 7.4°N, 340.4°E and its ejecta (Figure 13). The bottom of this exposure is separated by ~400 m elevation from the top of the lowermost olivine-rich layer in the channel, approximately 35 km away (Figure 13). The olivine-rich layer in the crater may be part of the same lower channel wall layer, and was uplifted during the impact that formed the crater, or it could represent a third layer. The exposure of the olivine-rich layers in the channel wall and distributed throughout the surrounding plains suggests that these layers extend at least 35 km in the north-south direction through the subsurface and predate both channel and crater formation.

4.1.2.1. Regional Geologic Context of the Olivine-Rich Unit

[50] The lower layer of the olivine-rich unit within the study region was previously mapped as part of a more areally extensive "Ares unit" by *Tanaka et al.* [2005] using thermophysical and morphologic characteristics. The Ares unit, which is distinguished by a comparatively high thermal inertia and erosion-resistant morphology extends beyond the study region to the west, east, and south, and is interpreted to have a hydrothermal or volcaniclastic origin [*Tanaka et al.*, 2005]. The possibility that the olivine-rich materials in upper Ares Vallis may extend beyond the study region as part of the Ares unit should be considered in order to best determine the mechanism and timing of emplacement of these materials. To the immediate west of the study region, there is an increase in dust cover which obscures the spectral character of the Ares unit. However, large outcrops (>30 km in one dimension) of the Ares unit outside of the study region with little dust cover are found in (1) Aram Chaos,

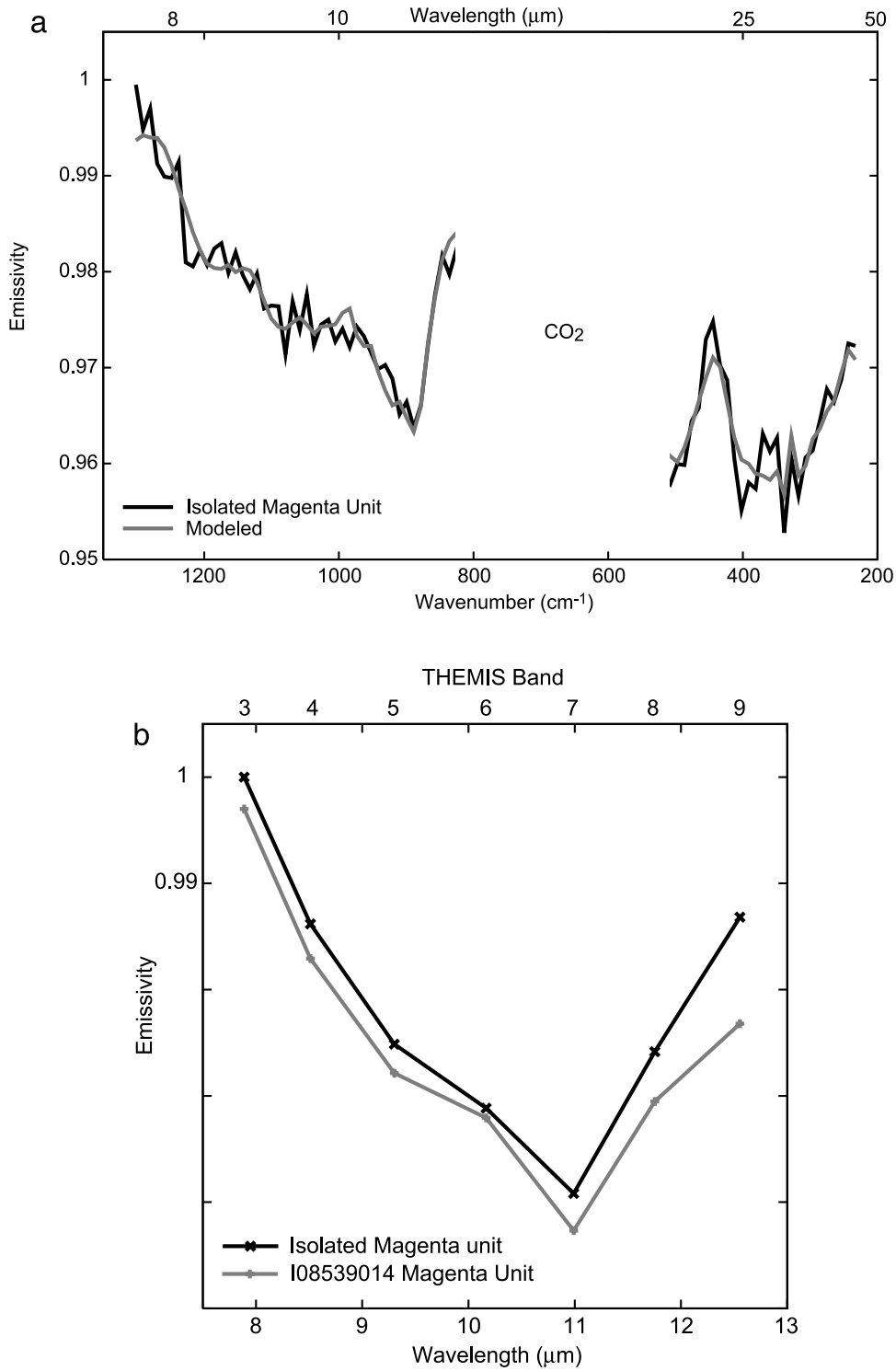

Figure 11. (a) Isolated surface spectrum for the DCS magenta unit and modeled spectrum. The corrected DCS magenta surface was derived by subtracting 50% of the DCS blue surface spectrum. The isolated magenta unit surface spectrum has higher noise due to the low number of spectra used in the average and also to the spectrum isolation process. See text for explanation. (b) Isolated magenta surface spectrum from Figure 11a, convolved to THEMIS spectral resolution. Compare with the THEMIS-derived surface emissivity from the magenta unit in I08539014 (average spectrum taken from area near M in Figure 2), shown here in gray. The overall match indicates that the TES surface spectrum for the magenta unit is well-isolated. The THEMIS surface spectrum has been contrast-adjusted for shape comparison; spectra are offset by 0.003 emissivity.

(2) an unnamed crater located at 344.1°E, 2.5°N, and (3) Chryse Planitia.

[51] The spectral properties of thermophysical and morphologic units in Aram Chaos, including the Ares unit mapped by *Tanaka et al.* [2005], were analyzed by T. D. Glotch and P. R. Christensen (Geologic and mineralogic mapping of Aram Chaos: Evidence for a water-rich history, submitted to *Journal of Geophysical Research*, 2004; hereinafter referred to as Glotch and Christensen, submitted manuscript, 2004). The Ares unit (referred to as the "Cap Unit" by Glotch and Christensen (submitted manuscript, 2004)), exhibits shallow spectral contrast in TES data relative to surrounding units and to Ares Vallis units, and is best modeled with ~30% pyroxene, 20% plagioclase, 20% high-silica components, and 10% sulfate. No olivine is required to model the surface emissivity (Glotch and Christensen, submitted manuscript, 2004). The higher sulfate abundance and albedo relative to its surroundings led Glotch and Christensen (submitted manuscript, 2004) to suggest that the Cap Unit may be a cemented clastic unit. A cemented material would be consistent with the higher thermal inertia values associated with this unit in Aram Chaos. In summary, the outcrop of the Ares unit in Aram Chaos [*Tanaka et al.*, 2005] is not spectrally similar to olivine-rich outcrops of the Ares unit in upper Ares Vallis.

[52] The Ares unit is exposed in the plains just to the east of the study region, as part of a ~250 m thick resistant layer filling the floor of an unnamed ~73 km-diameter crater located at 344.1°E, 2.5°N [*Tanaka et al.*, 2005]. Low-albedo portions of this area (TES albedo ≅ 0.125) examined with TES and THEMIS show very similar spectral character to the olivine-rich unit within the study region. Spectral ratios and linear deconvolution of TES spectra indicate that a similar concentration of olivine (20–25%) is present. This exposure of the Ares unit is located within ~100–300 meters elevation of the plains occurrences of olivine materials within the study region (Figures 13 and 14), and is considered to be part of the second olivine-rich layer discussed above.

[53] Finally, examination of a relatively dust-free (TES albedo ≅ 0.145) outcrop of the Ares unit in Chryse Planitia, located at ~325°E, 22°N reveals that the outcrops are generally more mafic than the surrounding low-albedo material, which is spectrally intermediate between Surface Types 1 and 2 [*Bandfield et al.*, 2000a, 2000b]. Spectral ratios between these outcrops and their surroundings indicate that olivine is present in the Ares unit in Chryse

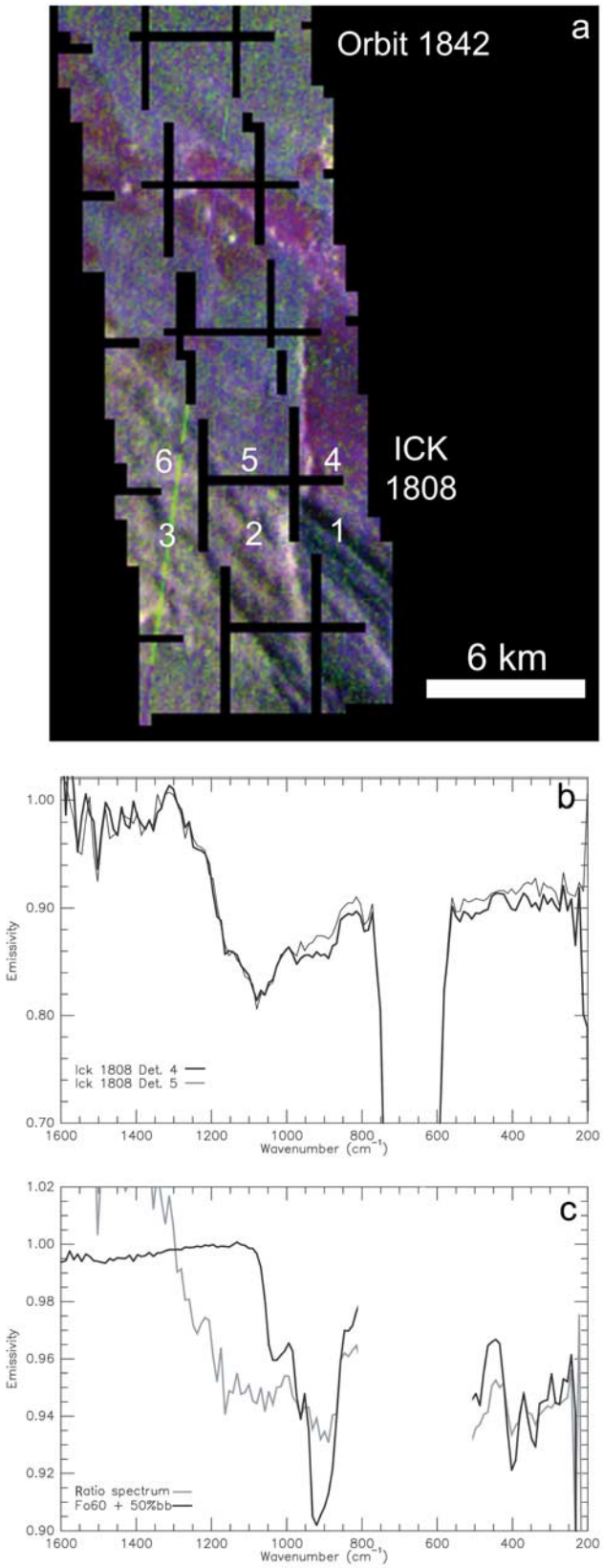

Figure 12. (a) Channel floor area in the THEMIS color mosaic (Figure 1), masked by the individual TES detector fields of view for MGS mapping phase orbit 1842, ICKs 1807–1810. TES detector fields of view for ICK 1808 are numbered 1–6. (b) TES effective emissivity spectra from ICK 1808. Detectors 4 and 5 are plotted. The detector 4 field of view is dominated by a magenta-hued surface in the THEMIS DCS mosaic, while detector 5 is dominated by a blue-hued surface. There are significant differences between the two spectra, especially in the wave number regions 300–550 cm^{-1} and 900 cm^{-1}. Spectral character at 1000 cm^{-1} and higher wave numbers is almost identical, indicating that the amount of atmospheric dust is not significantly different between the two detectors. (c) Ratio spectrum of the two emissivity spectra from Figure 12b, compared with a laboratory olivine (Fo_{60}) spectrum.

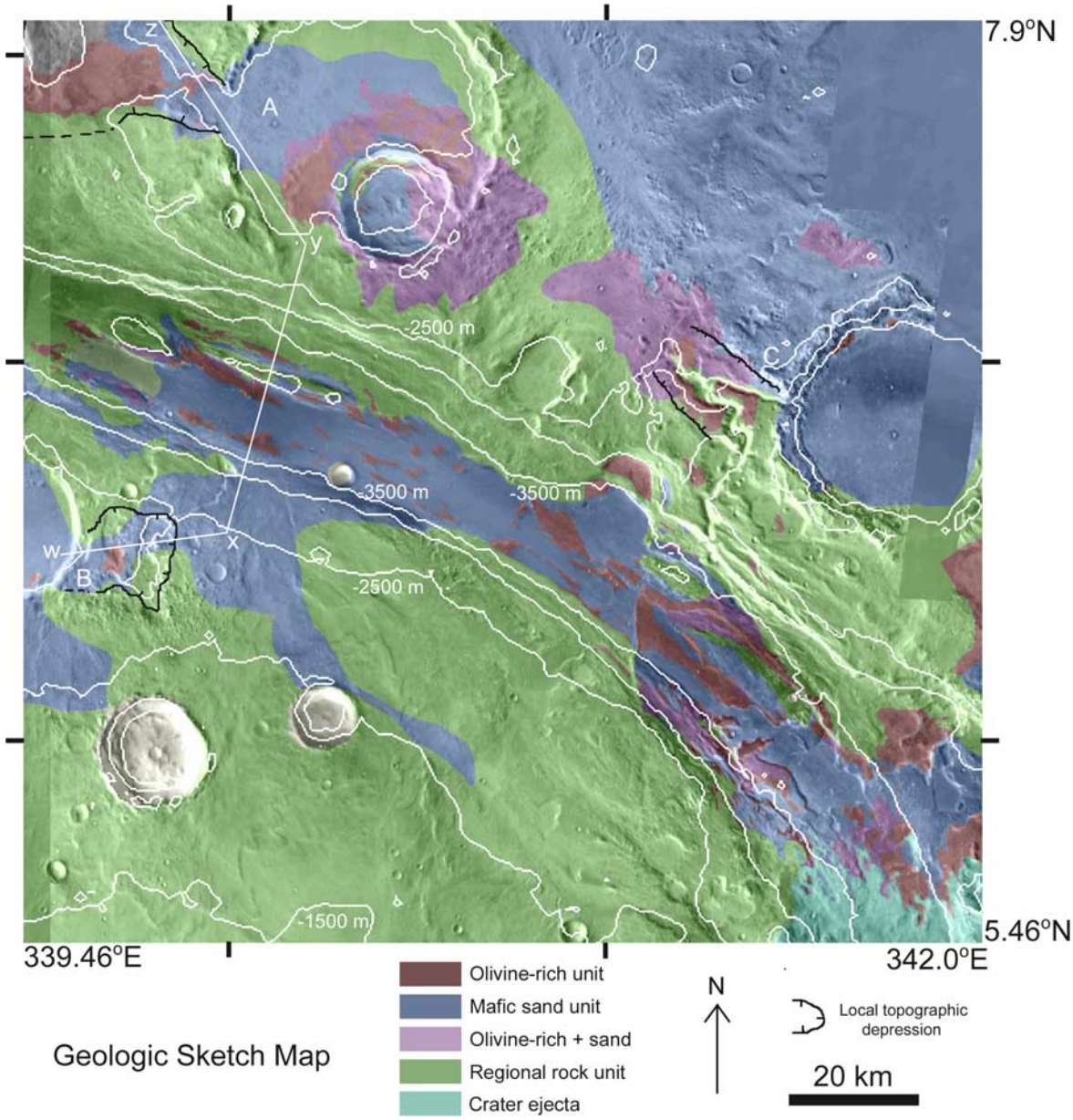

Figure 13. Geologic sketch map of spectral units in the Ares Vallis study region. Letters A–C indicate areas discussed in Figure 14. The topographic contour interval is 500 m. The w-z line is a representative transect for Figure 15.

Planitia; linear deconvolution of TES spectra from the outcrops place the maximum olivine concentration at ~10–15%. Overall, the depth of the features attributable to olivine in the ratio spectrum and the derived modal mineralogy from deconvolution indicate that the relative abundance of pyroxene and olivine is lower than that of the olivine-rich portions of the Ares unit in upper Ares Vallis. However, the presence of some olivine points to a possible genetic relationship between the Ares unit outcrops in Chryse Planitia with those in upper Ares Vallis.

4.1.2.2. Emplacement Mechanism for the Olivine-Rich Unit

[54] Emplacement mechanisms considered for the olivine-rich units are (1) volcanic flows, (2) younger igneous intrusions, and (3) sediments deposited in an aqueous or aeolian environment, representing time periods where pyroxene and olivine grains were more concentrated in the regional sand supply. A sedimentary origin would require at least two episodes of sedimentation that produced similar olivine-rich mineralogy, separated by volcanic activity and/or sedimentation that produced a ~1.4 km thick sequence of non-olivine-rich rocks; this scenario is considered the least likely. An intrusive origin could explain the observed stratigraphy within the study region by a single episode of olivine-enriched magmatism, such that some of the material intruded ancient rocks and some of the material pushed upward and either intruded at a shallower crustal level or was extruded at the surface. The proximity of the

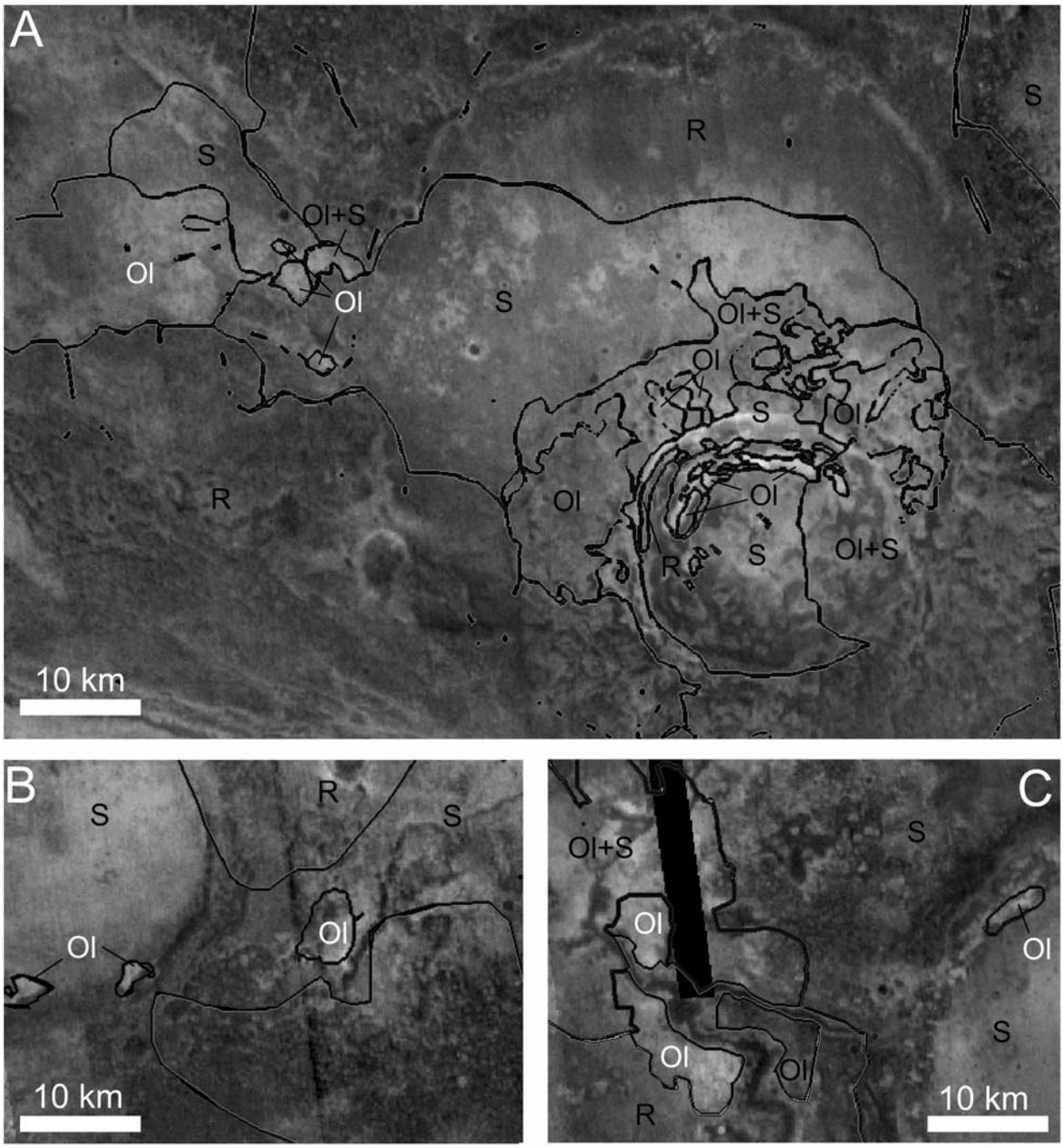

Figure 14. A, B, and C are the three areas where the magenta unit occurs outside of the outflow channel, in the surrounding plains (see Figure 13), within the study region. Mapped units are shown here overlain on portions of the THEMIS nighttime radiance mosaic. S, mafic sand unit; O, olivine-rich unit; R, regional rock unit; O+S, mixture of olivine-rich unit and mafic sand units (determined from spectral unit mapping). Olivine-rich surfaces that are associated with the relatively high thermal inertia material (500–550) are indicated with white letters. The sharp boundaries and relatively high thermal inertia values of these areas suggest that these are in-place units, rather than windblown sand.

olivine-rich materials found outside of the channel to large impact craters (25–45 km diameter, Figures 13 and 14) might suggest that fractures in the ancient rocks associated with the craters could have acted as conduits for the olivine magma. The association of the olivine-rich unit with the highest thermal inertia material suggests that this layer may be less porous, or less easily disaggregated, than its surrounding layers. Plutonic rocks tend to have lower primary porosity than sediments or extruded lavas [e.g., *Easterbrook*, 1993, p. 187].

[55] It is possible that the olivine-rich layers in Ares Vallis are part of a larger layered intrusion; however, there is a lack

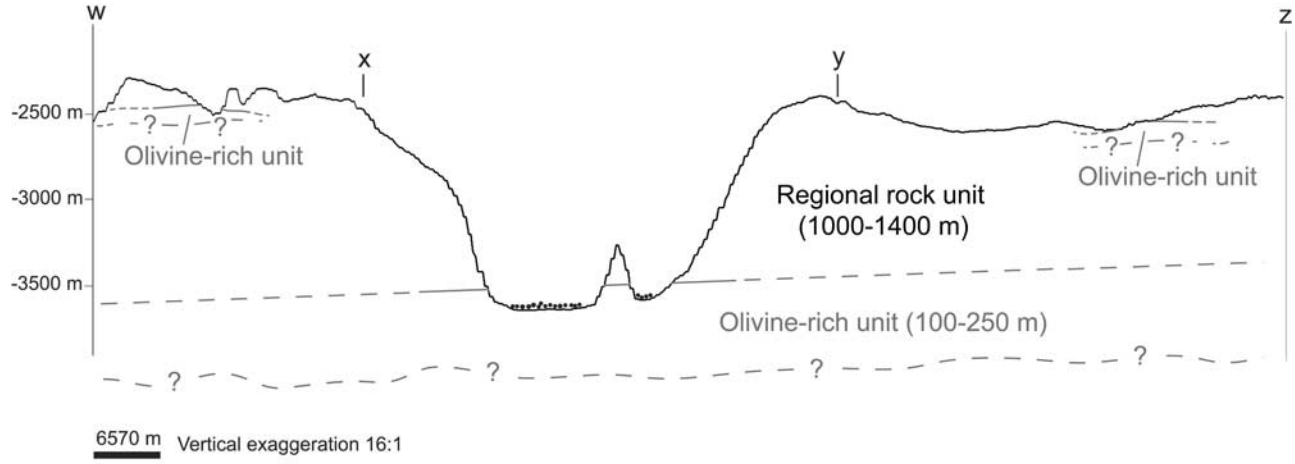

Figure 15. Generalized cross section of spectral units in the upper Ares Vallis study region. The tilt of layers shown may not be representative of actual layer geometry. Vertical exaggeration is approximately 16:1.

of associated layers of concentrated plagioclase or iron oxides, such as the anorthosite and chromitite layers found in the Skaergaard and Bushveld layered intrusions on Earth [e.g., *Eales and Cawthorn*, 1996; *McBirney*, 1996]. The layered rocks that vertically separate the two occurrences of olivine-rich materials are spectrally uniform, making the layered intrusion scenario less likely.

[56] Finally, although an intrusive origin could explain the observed stratigraphy with a single olivine-enriched magmatic episode, there is no evidence against extrusive emplacement of the olivine-rich materials nor is there a requirement for only one olivine-rich magmatic event. The full lateral extent of the olivine-rich units is unknown. It is likely that olivine-rich materials do extend beneath the dust cover to the immediate west of the study region, due to the continuity of the high thermal inertia mesa-forming materials associated with the olivine-rich surfaces within the study region (also mapped as the Ares unit by *Tanaka et al.* [2005]). However, it is not clear that the mafic exposures of the Ares unit as far west as Chryse Planitia (section 4.1.2.1) are related to the more olivine-rich exposures of the Ares unit in upper Ares Vallis. If these units formed from the same magmatic episode, then a solely intrusive origin for the olivine-rich materials in upper Ares Vallis seems less likely, due to the vast extent of the unit. The Ares unit exposures in Chryse Planitia are ~1500 km from those in upper Ares Vallis. This is almost a factor of 3 times greater than the largest dimension of exposed olivine-rich bedrock in Nili Fossae, which stretches at least ~540 km in the north-south direction [*Hamilton and Christensen*, 2005]. In summary, both extrusive and intrusive emplacement mechanisms are possible. If olivine-rich surfaces in upper Ares Vallis are genetically linked to the less olivine- and pyroxene-rich mafic outcrops in Chryse Planitia, then a solely intrusive scenario is unlikely.

4.1.3. Mafic Sand (DCS Blue)

[57] The mineralogy and derived chemistry (Table 2) of the blue spectral unit suggest a basaltic andesitic composition, with an elevated abundance of high-silica components such as silica coatings or glass. As mentioned above, the blue spectral unit is primarily associated with the lowest-albedo surfaces in the study region, and is interpreted as a loose sand unit (Figure 13). The sand component is likely to be keeping these areas free of dust via saltation; perhaps the channel geometry is facilitating the movement of sand by strong winds [e.g., *Christensen and Kieffer*, 1979]. For simplicity the blue spectral unit is hereafter referred to as the mafic sand unit.

[58] There are a few small areas (10–20 THEMIS pixels wide) within the blue spectral unit that appear associated with small outcrops of channel wall (Figure 13). These areas are too small to use TES albedo to distinguish whether they are exposed rock units of the same composition of the sand, or simply areas of concentrated sand. THEMIS visible images do not show relative darkening over those areas. No MOC images were available from these regions.

[59] The source of the mafic sand is not clear. Although there are a few areas that could potentially be in-place rock of the same composition, these are probably too small in extent to be the source for the entire mafic sand unit. One possible source of the sand is that it is derived from the regional rock unit. The primary difference in mineralogy between the regional rock unit and the sand unit is the relative abundance of high-silica material (Table 2). The ratio of plagioclase to pyroxene in these two units is nearly identical. In this scenario, at least part of the high-silica component of the rock unit is in the form of an amorphous silica coating or clay weathering product. As material is eroded from the walls via aeolian and mass-movement processes, sand particles of the wall rock are generated. The relative surface area of the coatings would be decreased by this process. However, because the sand unit still has a significant concentration of the high-silica material (25%), this would suggest that at least part of this material in the regional rock unit is in the form of a primary glass.

[60] One way that high-silica coatings might form is by silica liberation from dust and subsequent precipitation on the surface [e.g., *Kraft et al.*, 2003]. The regional rock unit and the olivine-rich unit have likely been exposed to similar physical and chemical conditions after channel formation. If part of the high-silica material is due to coatings, these coatings might be expected to be present on the olivine-rich

unit as well. Perhaps precipitated coatings were once present, but have been stripped by aeolian processes from the lowermost olivine unit, where the TES spectra were extracted, which is also coincidentally where the sand is more concentrated at the channel floor.

[61] A second possibility for the origin of the sand unit is that it is regionally derived from one or more bedrock sources that are now obscured by dust or sand. Spectral similarity to the TES Type 1 global end-member, which is derived from regional-scale averages and is found primarily in the southern highlands upstream from the study region [*Bandfield et al.*, 2000a], would support this. In this scenario, the high-silica component in this rock unit could be due entirely to primary glass.

4.1.4. Floor Materials

[62] The mafic sand unit obscures the composition of floor materials beneath it (e.g., Figure 8); however, the floor materials have unique features that suggest it may be a separate geologic unit than regional rock layers or olivine-rich rock materials. It is difficult to determine the stratigraphic relationship between the floor material (beneath the sand) and the lower layer of the olivine-rich unit. The contact between these two units may either represent a conformity that marks the top of the floor materials and bottom of the olivine-rich unit, or the floor materials may be younger than the olivine-rich materials, and the contact represents an embayment relationship. The floor materials appear less-cratered than the olivine-rich unit in THEMIS visible images, implying that these materials are younger and postdate channel formation. Inspection of the floor materials with MOC and THEMIS visible images reveals lobate flow fronts and dendritic patterns that may be surface cracks in some areas (Figures 7 and 8). These types of features, although found here at a slightly smaller scale, have previously been identified through detailed geologic mapping of the outflow terrain within Acidalia and Chryse Planitia regions by *Tanaka* [1997, 1999] and *Chapman and Tanaka* [2002] and were cited as evidence for debris flow activity. The Ares Vallis floor unit may have been emplaced by mass-wasting activity subsequent to the channel formation, similar to those previously mapped elsewhere in the outflow channel region. Other characteristic debris-flow features such as mud volcanoes [*Tanaka*, 1997] are not present, however, and there is no obvious head scarp nearby the study region. Failure scarps are found farther up the channel near Aram Chaos. *Tanaka* [1999] indicated that although most debris flow material is deposited in the outflow channel plains, some debris deposit remnants can be found in the channel floors.

4.2. Implications for the Geologic History of Ares Vallis

[63] The distribution of spectral units found strictly in the upper Ares Vallis study region are consistent with either an extrusive and/or intrusive origin for the olivine-rich materials (section 4.1.2.2). If these materials were emplaced as intrusions, this implies that a later stage of olivine-rich magmatism affected the Noachian crust in this region. Supporting evidence for late-stage magmatism in this region is the presence of chaos terrain, which is estimated to have formed during the late Hesperian during heightened tectonic and magmatic activity [*Maxwell and Picard*, 1974; *Masursky et al.*, 1977; *Scott and Tanaka*, 1986; *Rotto and Tanaka*, 1995; *Tanaka et al.*, 2005]. In addition, *Chapman and Tanaka* [2002] suggested that magma-ice interactions could be responsible for many of the features found in the Xanthe and Margaritifer Terrae regions on Mars. It is possible that the magmatic activity that produced the chaos terrain in this region may be related to the magmatic activity that produced the olivine-rich layers. If, however, the unit largely consists of volcanic flows, with or without associated intrusions, the implication would be that periodic olivine-enriched magmatism occurred throughout the formation of the Noachian and Hesperian crust in this region. Regardless of an extrusive or intrusive origin, this magmatism is constrained to have occurred no later than the late Hesperian (~3 Ga [*Hartmann and Neukum*, 2001]).

[64] Basaltic minerals that are most susceptible to chemical alteration are olivine and pyroxene [e.g., *Goldich*, 1938; *Brady and Walther*, 1989; *Burns*, 1993]. Although the initial amount of crystallized olivine is unknown, the presence of a lithology that still contains ~25% olivine indicates that chemical weathering has been a minor process since these rocks formed. Limited chemical weathering has been suggested for other olivine-rich terrains on Mars [*Christensen et al.*, 2003; *Hamilton et al.*, 2003; *Hoefen et al.*, 2003]. Preliminary calculations by *Stopar et al.* [2003] indicate that 1 mm olivine grains completely dissolve within timeframes on the order of 10^0 to 10^4 years; however, olivine dissolution rates can be significantly slower under terrestrial field versus lab conditions, and more work is needed to quantify the kinetics of olivine dissolution under Martian conditions [*Tosca et al.*, 2004]. Despite these uncertainties, a general conclusion can be made that warm and wet environmental conditions have been severely limited in the Ares Vallis region since the time of crystallization (at least ~3 Ga), given that such a large concentration of olivine (~25%) and pyroxene (~45%) remains. In addition, if a portion of the high-silica component in the regional wall rock is due to primary glass, this would also suggest that chemical weathering under wet conditions has been limited. The mineral assemblages present in Ares Vallis are not, however, inconsistent with outflow models that only require short-lived periods of fluvial channel incision [e.g., *Baker et al.*, 1992; *Carr*, 1996].

[65] The olivine-rich unit is the lowest exposed bedrock layer that can be distinguished in the channel; near the mouth of Aram Chaos it forms part of the floor material of the channel. The thermophysical and morphologic properties of the olivine-rich unit suggest that this material is more resistant to erosion than the regional rock unit. The position of this exposed layer at the bottom of the channel suggests that the relatively resistant olivine-rich unit may have acted to inhibit continued channel incision.

4.3. Global Distribution of Olivine-Bearing Units

[66] The Ares Vallis olivine-rich unit is one of several olivine-bearing terrains that have been identified on Mars. Olivine-rich surfaces in Nili Fossae [*Hoefen et al.*, 2003] extend at least ~113,000 km^2 in area [*Hamilton and Christensen*, 2005]. The olivine compositions in Nili Fossae range from $<Fo_{40}$ to Fo_{70} [*Hamilton et al.*, 2003; *Hoefen et al.*, 2003; *Hamilton and Christensen*, 2005]; however, $\sim Fo_{65}$ is the most areally extensive olivine composition. The modal mineralogy in Nili Fossae consists primarily of

olivine (~30%) [*Hoefen et al.*, 2003], plagioclase (~15%), and pyroxene (~15%). In Ganges Chasma, olivine-rich materials are exposed as a 50–100 m thick continuous layer that extends across an area at least 30 × 100 km, with an olivine concentration of >20% and a composition of ~Fo_{65} [*Christensen et al.*, 2003, 2005]. Finally, olivine-rich rocks and soils have been identified at Gusev crater [*Bell et al.*, 2004; *Christensen et al.*, 2004b; *Gellert et al.*, 2004; *McSween et al.*, 2004; *Morris et al.*, 2004]. Initial results from the MiniTES experiment on the Spirit Rover suggest that dark rocks and disturbed soils on the Gusev plains consist of ~10–15% olivine of composition Fo_{35-60} [*Christensen et al.*, 2004b]. Alpha Proton X-Ray Spectrometer (APXS) measurements of the deepest RAT-brushed surfaces of 3 representative rocks give an average chemical composition of ~45.5 SiO_2, ~10.8% Al_2O_3, 18.0% FeO*, and ~11.4% MgO [*Gellert et al.*, 2004; *McSween et al.*, 2004]. Normative mineralogy calculated from these APXS analyses suggest an olivine abundance of 26–35%, with an olivine composition ranging from Fo_{51-55} [*McSween et al.*, 2004]. Results from both the MiniTES and APXS instruments suggest that plagioclase (~40%) and pyroxene (~13–45%) are the other dominant mineralogic components of the dark rocks and soils.

[67] From a mineralogic standpoint, the Ares Vallis olivine unit is different than the previously identified olivine-bearing terrains in that it generally has a higher pyroxene concentration and a significantly lower plagioclase concentration, making it the most mafic of the units identified to date. The total concentration of olivine is similar between Ares Vallis, Nili Fossae, Ganges and Gusev basalts, however, varying from ~20–35%. Finally, the composition of Ares Vallis olivine (~Fo_{60}) is similar to that of Nili Fossae and Ganges Chasma, and within the range of that reported for Gusev basalts.

[68] The olivine-bearing units identified to date are confined to the ancient cratered terrain, with probable ages that range from Noachian to Hesperian. They are not isolated to a single volcanic province, but rather are observed in scattered exposures throughout the equatorial region. The existence of widespread examples of olivine-rich (>20 vol.%) basaltic units suggests that one global episode or several unrelated episodes of olivine-rich igneous activity occurred during the first ~1.5 Gyr of crust formation, but no later. In general, if these compositions represent melt compositions, instead of cumulates, the olivine-rich magmas are more primitive than the majority of the exposed Martian crustal compositions (basalts to basaltic andesites [*Bandfield et al.*, 2000a; *McSween et al.*, 2003]). Production of these unique lithologies may be analogous to that of terrestrial komatiites, not by direct comparison of composition, but rather in the sense that they are restricted to the early portion of the planet's history. As with komatiites, the relatively primitive compositions of the olivine-rich terrains may indicate very different mantle conditions, such as higher temperatures [e.g., *Hess*, 1989, pp. 276–285; *Basaltic Volcanism Study Project* (*BVSP*), 1981, pp. 5–29]. Higher mantle temperatures (leading to larger degrees of partial melting) are consistent with most Martian thermal evolution models, which show a general decline in mantle temperatures with time, although there is some question as to how rapidly the decline occurred during early planet history [e.g., *Schubert and Spohn*, 1990; *Grasset and Paramentier*, 1998; *Nimmo and Stevenson*, 2000; *Zuber*, 2001; *Hauck and Phillips*, 2002]. Alternatively, these olivine-rich compositions may reflect a difference in the composition of the mantle source, such as extent of depletion [e.g., *BVSP*, 1981, pp. 5–29]. The variations in modal mineralogy between each of these olivine-rich terrains may be due to differences in melt fraction and/or the composition of the mantle sources, and/or modification of the olivine-rich magmas through assimilation or fractionation [e.g., *BVSP*, 1981, pp. 399–482]. The identification of several olivine-rich (>20%) terrains distributed sparsely throughout the cratered southern hemisphere suggests that these lithologies may be common at depth in the ancient crust.

5. Conclusions

[69] Detailed spectral analysis and mapping of the upper Ares Vallis outflow channel and surrounding plains have shown the following:

[70] 1. An olivine- and pyroxene-rich unit occurs in two layers that are vertically separated by ~1–1.4 km of regional mafic crustal rocks. These layers may be extrusive and/or intrusive in origin, and are at least ~3 Ga.

[71] 2. The majority of the crust exposed in the walls of Ares Vallis and throughout this region is mafic in composition, consisting of plagioclase, clinopyroxene, and a high-silica (Si/O > ~0.35) component that is primary glass and/or a secondary high-silica phase.

[72] 3. The Ares Vallis region experienced either a single stage or repeated episodes of olivine-enriched magmatism during the formation of the regional Noachian/Hesperian crust. The identification of similar layered compositional variations in Ares Vallis, Ganges Chasma [*Christensen et al.*, 2003], and Nili Fossae [*Hoefen et al.*, 2003; *Hamilton and Christensen*, 2004] suggests that a unique olivine-rich (>20%) igneous component may be widespread within ancient terrains, and that subkilometer-scale vertical heterogeneity in the crust may be common on Mars. This heterogeneity may have been produced by temporal variations in the composition or temperature of the source regions for the olivine-rich magmas during the formation of the early crust.

[73] 4. A significant amount of low albedo material is concentrated in the channel floor and surrounding plains areas. Similarity in mineralogy between the sand unit and the mafic wall rock suggests that the sand is derived from the regional mafic crust.

[74] 5. The exposure of materials >3 Gyr in age that contain ~25% olivine demonstrates that chemical weathering has been limited in this region and suggests that warm/wet conditions, including the formation of Ares Vallis, were limited in duration.

[75] **Acknowledgments.** We thank the THEMIS mission planners Kelly Bender, Laural Cherednik, and Andras Dombovari for graciously acquiring our requested images. Vicky Hamilton kindly provided the olivine spectra used in this work and also contributed to discussions which improved this manuscript. We appreciate the help of Christopher Edwards and Keith Nowicki, whose contribution was essential in creating the final versions of IR mosaics and DCS images presented in this work. Tim Glotch provided a helpful review of an early version of this manuscript, and Mike Wyatt contributed useful discussions. We are grateful to Nathan Bridges and Ken Tanaka for thorough formal reviews and suggestions. Finally, we

thank Greg Mehall and the THEMIS instrument development team at Raytheon Santa Barbara Remote Sensing and Ben Steinberg, Michael Weiss-Malik, Noel Gorelick, and Saadat Anwar for development and assistance in using the JMARS data analysis software.

References

Baker, V. R., and D. J. Milton (1974), Erosion by catastrophic floods on Mars and Earth, *Icarus*, *23*(1), 27–41.

Baker, V. R., M. H. Carr, V. C. Gulick, C. R. Williams, and M. S. Marley (1992), Channels and valley networks, in *Mars*, edited by H. H. Kieffer et al., pp. 493–522, Univ. of Ariz. Press, Tucson.

Bandfield, J. L. (2002), Global mineral distributions on Mars, *J. Geophys. Res.*, *107*(E6), 5042, doi:10.1029/2001JE001510.

Bandfield, J. L., and M. D. Smith (2003), Multiple emission angle surface-atmosphere separations of Thermal Emission Spectrometer data, *Icarus*, *161*(1), 47–65.

Bandfield, J. L., V. E. Hamilton, and P. R. Christensen (2000a), A global view of Martian surface compositions from MGS-TES, *Science*, *287*(5458), 1626–1630.

Bandfield, J. L., P. R. Christensen, and M. D. Smith (2000b), Spectral data set factor analysis and end-member recovery: Application to analysis of Martian atmospheric particulates, *J. Geophys. Res.*, *105*(E4), 9573–9587.

Bandfield, J. L., V. E. Hamilton, P. R. Christensen, and H. Y. McSween Jr. (2004a), Identification of quartzofeldspathic materials on Mars, *J. Geophys. Res.*, *109*, E10009, doi:10.1029/2004JE002290.

Bandfield, J. L., D. Rogers, M. D. Smith, and P. R. Christensen (2004b), Atmospheric correction and surface spectral unit mapping using Thermal Emission Imaging System data, *J. Geophys. Res.*, *109*, E10008, doi:10.1029/2004JE002289.

Banin, A., B. C. Clark, and H. Wanke (1992), Surface chemistry and mineralogy, in *Mars*, edited by H. H. Kieffer et al., pp. 594–625, Univ. of Ariz. Press, Tucson.

Basaltic Volcanism Study Project (BVSP) (1981), *Basaltic Volcanism on the Terrestrial Planets*, Elsevier, New York.

Bell, J. F., et al. (2004), Pancam multispectral imaging results from the Spirit Rover at Gusev crater, *Science*, *305*(5685), 800–806.

Blaney, D. L., D. A. Glenar, and G. L. Bjorker (2003), High spectral resolution spectroscopy of Mars from 2 to 4 microns: Surface mineralogy and the atmosphere, in *Sixth International Conference on Mars* [CD-ROM], abstract 3237, Lunar and Planet. Inst., Houston, Tex.

Brady, P. V., and J. V. Walther (1989), Controls on silicate dissolution rates in neutral and basic pH solutions at 25C, *Geochim. Cosmochim. Acta*, *53*, 2823–2830.

Burns, R. G. (1993), Rates and mechanisms of chemical weathering of ferromagnesian silicate minerals on Mars, *Geochim. Cosmochim. Acta*, *57*, 4555–4574.

Carr, M. H. (1979), Formation of Martian flood features by release of water from confined aquifers, *J. Geophys. Res.*, *84*(6), 2995–3007.

Carr, M. H. (1996), *Water on Mars*, Oxford Univ. Press, New York.

Chapman, M. G., and J. S. Kargel (1999), Observations at the Mars Pathfinder site: Do they provide "unequivocal" evidence of catastrophic flooding?, *J. Geophys. Res.*, *104*(E4), 8671–8678.

Chapman, M. G., and K. L. Tanaka (2002), Related magma-ice interactions: Possible origins of chasmata, chaos, and surface materials in Xanthe, Margaritifer, and Meridiani Terrae, Mars, *Icarus*, *155*(2), 324–339.

Christensen, P. R. (1986), The spatial distribution of rocks on Mars, *Icarus*, *68*, 217–238.

Christensen, P. R. (1998), Variations in Martian surface composition and cloud occurrence determined from thermal infrared spectroscopy: Analysis of Viking and Mariner 9 data, *J. Geophys. Res.*, *103*(E1), 1733–1746.

Christensen, P. R., and H. H. Kieffer (1979), Moderate resolution thermal mapping of Mars: The channel terrain around the Chryse Basin, *J. Geophys. Res.*, *84*, 8233–8238.

Christensen, P. R., et al. (1992), Thermal Emission Spectrometer Experiment: Mars Observer Mission, *J. Geophys. Res.*, *97*(E5), 7719–7734.

Christensen, P. R., et al. (2000a), Detection of crystalline hematite mineralization on Mars by the Thermal Emission Spectrometer: Evidence for near-surface water, *J. Geophys. Res.*, *105*(E4), 9623–9642.

Christensen, P. R., J. L. Bandfield, M. D. Smith, V. E. Hamilton, and R. N. Clark (2000b), Identification of a basaltic component on the Martian surface from Thermal Emission Spectrometer data, *J. Geophys. Res.*, *105*(E4), 9609–9621.

Christensen, P. R., J. L. Bandfield, V. E. Hamilton, D. A. Howard, M. D. Lane, J. L. Piatek, S. W. Ruff, and W. L. Stefanov (2000c), A thermal emission spectral library of rock-forming minerals, *J. Geophys. Res.*, *105*(E4), 9735–9739.

Christensen, P. R., R. V. Morris, M. D. Lane, J. L. Bandfield, and M. C. Malin (2001a), Global mapping of Martian hematite mineral deposits: Remnants of water-driven processes on early Mars, *J. Geophys. Res.*, *106*(E10), 23,873–23,885.

Christensen, P. R., et al. (2001b), Mars Global Surveyor Thermal Emission Spectrometer experiment: Investigation description and surface science results, *J. Geophys. Res.*, *106*(E10), 23,823–23,871.

Christensen, P. R., et al. (2003), Morphology and composition of the surface of Mars: Mars Odyssey THEMIS results, *Science*, *300*(5628), 2056–2061.

Christensen, P. R., et al. (2004a), The Thermal Emission Imaging System (THEMIS) for the Mars 2001 Odyssey Mission, *Space Sci. Rev.*, *110*(1–2), 85–130.

Christensen, P. R., et al. (2004b), Initial results from the Mini-TES experiment in Gusev crater from the Spirit rover, *Science*, *305*(5685), 837–842.

Christensen, P. R., et al. (2005), Evidence for igneous diversity and magmatic evolution on Mars from infrared spectral observations, *Nature*, in press.

Cutts, J. A., and K. R. Blasius (1981), Origin of Martian outflow channels: The eolian hypothesis, *J. Geophys. Res.*, *86*(6), 5075–5102.

Eales, H. V., and R. G. Cawthorn (1996), The Bushveld Complex, in *Layered Intrusions*, edited by R. G. Cawthorn, pp. 181–230, Elsevier, New York.

Easterbrook, D. J. (1993), *Surface Processes and Landforms*, 520 pp., Prentice-Hall, Upper Saddle River, N. J.

Edgett, K. S., and P. R. Christensen (1991), The particle size of Martian aeolian dunes, *J. Geophys. Res.*, *96*(E5), 22,765–22,776.

Fergason, R. L., and P. R. Christensen (2003), Thermal inertia using THEMIS infrared data, *Lunar Planet. Sci.*, *XXXIV*, abstract 1785.

Folco, L., I. A. Franchi, M. D'Orazio, S. Rocchi, and L. Schultz (2000), A new Martian meteorite from the Sahara: The shergottite Dar al Gani 489, *Meteorit. Planet. Sci.*, *35*, 827–839.

Gellert, R., et al. (2004), Chemistry of rocks and soils in Gusev crater from the alpha particle x-ray spectrometer, *Science*, *305*(5685), 829–832.

Gillespie, A. R. (1992a), Enhancement of multispectral thermal infrared images: Decorrelation contrast stretching, *Remote Sens. Environ.*, *42*(2), 147–155.

Gillespie, A. R. (1992b), Spectral mixture analysis of multispectral thermal infrared images, *Remote Sens. Environ.*, *42*(2), 137–145.

Gillespie, A. R., A. B. Kahle, and R. E. Walker (1986), Color enhancement of highly correlated images. I. Decorrelation and HSI contrast stretches, *Remote Sens. Environ.*, *20*, 209–235.

Goldich, S. (1938), A study of rock weathering, *J. Geol.*, *46*, 17–58.

Golombek, M. P., R. A. Cook, H. J. Moore, and T. J. Parker (1997), Selection of the Mars Pathfinder landing site, *J. Geophys. Res.*, *102*(E2), 3967–3988.

Gooding, J. L. (1992), Physical and chemical weathering, in *Mars*, edited by H. H. Kieffer et al., pp. 626–651, Univ. of Ariz. Press, Tucson.

Gorelick, N., M. Weiss-Malik, B. Steinberg, and S. Anwar (2003), JMARS: A multimission data fusion application, *Lunar Planet. Sci.*, *XXXIV*, abstract 257.

Grasset, O., and E. M. Parmentier (1998), Thermal convection in a volumetrically heated, infinite Prandtl number fluid with strongly temperature-dependent viscosity: Implications for planetary thermal evolution, *J. Geophys. Res.*, *103*, 18,171–18,181.

Hamilton, V. E., and P. R. Christensen (2000), Determining the modal mineralogy of mafic and ultramafic igneous rocks using thermal emission spectroscopy, *J. Geophys. Res.*, *105*(E4), 9717–9733.

Hamilton, V. E., and P. R. Christensen (2004), Green Mars: Geologic characteristics of olivine-bearing terrains as observed by THEMIS, MOC and MOLA, *Lunar Planet. Sci.*, *XXXV*, abstract 2131.

Hamilton, V. E., and P. R. Christensen (2005), Evidence for extensive, olivine-rich bedrock on Mars, *Geology*, in press.

Hamilton, V. E., M. B. Wyatt, H. Y. McSween, and P. R. Christensen (2001), Analysis of terrestrial and Martian volcanic compositions using thermal emission spectroscopy: 2. Application to Martian surface spectra from the Mars Global Surveyor Thermal Emission Spectrometer, *J. Geophys. Res.*, *106*(E7), 14,733–14,746.

Hamilton, V. E., P. R. Christensen, and H. Y. McSween (2002), Global constraints on the source regions of Martian meteorites from MGS TES data, *Meteorit. Planet. Sci.*, *37*(7), A59–A59.

Hamilton, V. E., P. R. Christensen, H. Y. McSween, and J. L. Bandfield (2003), Searching for the source regions of Martian meteorites using MGS TES: Integrating Martian meteorites into the global distribution of igneous materials on Mars, *Meteorit. Planet. Sci.*, *38*(6), 871–885.

Hartmann, W. K., and G. Neukum (2001), Cratering chronology and the evolution of Mars, *Space Sci. Rev.*, *96*(1–4), 165–194.

Hauck, S. A., II, and R. J. Phillips (2002), Thermal and crustal evolution of Mars, *J. Geophys. Res.*, *107*(E7), 5052, doi:10.1029/2001JE001801.

Hess, P. C. (1989), *Origins of Igneous Rocks*, 336 pp., Harvard Univ. Press, Cambridge, Mass.

Hoefen, T. M., R. N. Clark, J. L. Bandfield, M. D. Smith, J. C. Pearl, and P. R. Christensen (2003), Discovery of olivine in the Nili Fossae region of Mars, *Science*, *302*(5645), 627–630.

Jakosky, B. M., and M. T. Mellon (2001), High-resolution thermal inertia mapping of Mars: Sites of exobiological interest, *J. Geophys. Res.*, *106*(E10), 23,887–23,907.

Jakosky, B. M., M. T. Mellon, H. H. Kieffer, P. R. Christensen, E. S. Varnes, and S. W. Lee (2000), The thermal inertia of Mars from the Mars Global Surveyor Thermal Emission Spectrometer, *J. Geophys. Res.*, *105*(E4), 9643–9652.

Kahle, A. B. (1987), Surface emittance, temperature, and thermal inertia derived from Thermal Infrared Multispectral Scanner (TIMS) data for Death Valley, California, *Geophysics*, *52*(7), 858–874.

Kieffer, H. H., T. Z. Martin, A. B. Peterfreund, B. M. Jakosky, E. D. Miner, and F. D. Palluconi (1977), Thermal and albedo mapping of Mars during the Viking primary mission, *J. Geophys. Res.*, *82*, 4249–4291.

Koeppen, W. C., and V. E. Hamilton (2004), Volcanism and/or aqueous alteration on Mars: Constraints on distinguishing glass and phyllosilicate in the thermal infrared, *Lunar Planet. Sci.*, *XXXV*, abstract 1457.

Kraft, M. D., J. R. Michalski, and T. G. Sharp (2003), Effects of pure silica coatings on thermal emission spectra of basaltic rocks: Considerations for Martian surface mineralogy, *Geophys. Res. Lett.*, *30*(24), 2288, doi:10.1029/2003GL018848.

Le Bas, M. J., R. W. Le Maitre, A. L. Streckheisen, and B. Zanettin (1986), A chemical classification of volcanic rocks based on the total alkali-silica diagram, *J. Petrol.*, *27*, 745–750.

Lyon, R. J. P. (1965), Analysis of rocks by spectral infrared emission (8 to 25 microns), *Econ. Geol.*, *60*, 715–736.

Malin, M. C., and K. S. Edgett (2001), Mars Global Surveyor Mars Orbiter Camera: Interplanetary cruise through primary mission, *J. Geophys. Res.*, *106*(E10), 23,429–23,570.

Masursky, H., K. Blasius, M. Carr, J. Cutts, R. Greeley, and J. Guest (1977), Viking view of evolution of crust of Mars, *Abstr. Pap. Am. Chem. Soc.*, *173*, 55.

Maxwell, T. A., and M. D. Picard (1974), Evidence of subsurface water in equatorial regions of Mars, *AAPG Bull.*, *58*, 915.

McBirney, A. R. (1996), The Skaergaard Intrusion, in *Layered Intrusions*, edited by R. G. Cawthorn, pp. 147–180, Elsevier, New York.

McLennan, S. M. (2003), Sedimentary silica on Mars, *Geology*, *31*(4), 315–318.

McSween, H. Y., Jr. (1994), What we have learned about Mars from SNC meteorites, *Meteoritics*, *29*(6), 757–779.

McSween, H. Y., Jr., T. L. Grove, and M. B. Wyatt (2003), Constraints on the composition and petrogenesis of the Martian crust, *J. Geophys. Res.*, *108*(E12), 5135, doi:10.1029/2003JE002175.

McSween, H. Y., et al. (2004), Basaltic rocks analyzed by the Spirit rover in Gusev Crater, *Science*, *305*(5685), 842–845.

Mellon, M. T., B. M. Jakosky, H. H. Kieffer, and P. R. Christensen (2000), High-resolution thermal inertia mapping from the Mars Global Surveyor Thermal Emission Spectrometer, *Icarus*, *148*(2), 437–455.

Michalski, J. R., M. D. Kraft, T. Diedrich, T. G. Sharp, and P. R. Christensen (2003), Thermal emission spectroscopy of the silica polymorphs and considerations for remote sensing of Mars, *Geophys. Res. Lett.*, *30*(19), 2008, doi:10.1029/2003GL018354.

Michalski, J. R., M. D. Kraft, T. G. Sharp, L. B. Williams, and P. R. Christensen (2004), Emission spectroscopy of smectites: Implications for the TES andesite-weathered basalt debate, *Lunar Planet. Sci.*, *XXXV*, abstract 1401.

Michalski, J. R., M. D. Kraft, T. G. Sharp, L. B. Williams, and P. R. Christensen (2005), Mineralogical constraints on the high-silica Martian surface component observed by TES: Clay-rich mineralogy does not sufficiently explain the Acidalia Planitia-type spectra, *Icarus*, *174*(1), 161–177.

Morris, R. V., T. G. Graff, S. A. Mertzman, M. D. Lane, and P. R. Christensen (2003), Palagonitic (not andesitic) Mars: Evidence from thermal emission and VNIR spectra of palagonitic alteration rinds on basaltic rock, in *Sixth International Conference on Mars* [CD-ROM], abstract 3211, Lunar and Planet. Inst., Houston, Tex.

Morris, R. V., et al. (2004), Mineralogy at Gusev crater from the Mossbauer spectrometer on the Spirit rover, *Science*, *305*(5685), 833–836.

Morse, S. A. (1996), Kiglapait mineralogy. 3. Olivine compositions and Rayleigh fractionation models, *J. Petrol.*, *37*(5), 1037–1061.

Nimmo, F., and D. J. Stevenson (2000), Influence of early plate tectonics on the thermal evolution and magnetic field of Mars, *J. Geophys. Res.*, *105*(E5), 11,969–11,979.

Nowicki, S. A., and P. R. Christensen (2003), Understanding rocky surfaces on Mars: Observations from TES and THEMIS, in *Eos Trans. AGU*, *84*(46), Fall Meet. Suppl., Abstract P22A-0063.

Ramsey, M. S. (2002), Ejecta distribution patterns at Meteor Crater, Arizona: On the applicability of lithologic end-member deconvolution for spaceborne thermal infrared data of Earth and Mars, *J. Geophys. Res.*, *107*(E8), 5059, doi:10.1029/2001JE001827.

Ramsey, M. S., and P. R. Christensen (1998), Mineral abundance determination: Quantitative deconvolution of thermal emission spectra, *J. Geophys. Res.*, *103*(B1), 577–596.

Ramsey, M. S., P. R. Christensen, N. Lancaster, and D. A. Howard (1999), Identification of sand sources and transport pathways at the Kelso Dunes, California, using thermal infrared remote sensing, *Geol. Soc. Am. Bull.*, *111*(5), 646–662.

Rogers, D., and P. R. Christensen (2003), Age relationship of basaltic and andesitic surface compositions on Mars: Analysis of high-resolution TES observations of the northern hemisphere, *J. Geophys. Res.*, *108*(E4), 5030, doi:10.1029/2002JE001913.

Rogers, D., J. L. Bandfield, and P. R. Christensen (2003), Global bedrock composition mapping on Mars using THEMIS and TES data, *Lunar Planet. Sci.*, *XXXIV*, abstract 2082.

Rotto, S., and K. L. Tanaka (1995), Geologic/geomorphic map of the Chryse Planitia region of Mars, *U.S. Geol. Surv. Misc. Invest. Ser., Map I-2441*.

Ruff, S. W. (2003), Basaltic andesite or weathered basalt: A new assessment, in *Sixth International Conference on Mars* [CD-ROM], abstract 3258, Lunar and Planet. Inst., Houston, Tex.

Ruff, S. W. (2004), Spectral evidence for zeolite in the dust on Mars, *Icarus*, *168*(1), 131–143.

Ruff, S. W., and P. R. Christensen (2002a), THEMIS multi-spectral views of compositional heterogeneity in Nili Patera Caldera, *Eos Trans. AGU*, *83*(47), Fall Meet. Suppl., Abstract P11B-10.

Ruff, S. W., and P. R. Christensen (2002b), Bright and dark regions on Mars: Particle size and mineralogical characteristics based on Thermal Emission Spectrometer data, *J. Geophys. Res.*, *107*(E12), 5127, doi:10.1029/2001JE001580.

Ruff, S. W., P. R. Christensen, R. N. Clark, H. H. Kieffer, M. C. Malin, J. L. Bandfield, B. M. Jakosky, M. D. Lane, M. T. Mellon, and M. A. Presley (2001), Mars' "White Rock" feature lacks evidence of an aqueous origin: Results from Mars Global Surveyor, *J. Geophys. Res.*, *106*(E10), 23,921–23,927.

Schubert, G., and T. Spohn (1990), Thermal history of Mars and the sulfur content of its core, *J. Geophys. Res.*, *95*(B9), 14,095–14,104.

Scott, D. H., and K. L. Tanaka (1986), Geologic map of the western equatorial region of Mars, *U.S. Geol. Surv. Misc. Invest. Ser, Map I-1802A*.

Sharp, R. P. (1973), Mars: Fretted and chaotic terrains, *J. Geophys. Res.*, *78*(20), 4073–4083.

Smith, D. E., et al. (2001), Mars Orbiter Laser Altimeter: Experiment summary after the first year of global mapping of Mars, *J. Geophys. Res.*, *106*(E10), 23,689–23,722.

Smith, M. D., J. L. Bandfield, and P. R. Christensen (2000), Separation of atmospheric and surface spectral features in Mars Global Surveyor Thermal Emission Spectrometer (TES) spectra, *J. Geophys. Res.*, *105*(E4), 9589–9607.

Soderblom, L. A. (1992), The composition and mineralogy of the Martian surface from spectroscopic observations: 0.3 microns to 50 microns, in *Mars*, edited by H. H. Kieffer et al., pp. 557–593, Univ. of Ariz. Press, Tucson.

Stopar, J. D., G. J. Taylor, V. E. Hamilton, L. Browning, and D. Pickett (2003), Maximum rates of olivine dissolution on Mars, in *Sixth International Conference on Mars* [CD-ROM], abstract 3151, Lunar and Planet. Inst., Houston, Tex.

Streckheisen, A. L. (1974), Classification and nomenclature of plutonic rocks, *Geol. Rundsch.*, *63*(2), 773–786.

Tanaka, K. L. (1986), The stratigraphy of Mars, *Proc. Lunar Planet. Sci. Conf. 17th*, Part 1, *J. Geophys. Res.*, *91*, suppl., E139–E158.

Tanaka, K. L. (1997), Sedimentary history and mass flow structures of Chryse and Acidalia Planitiae, Mars, *J. Geophys. Res.*, *102*(E2), 4131–4149.

Tanaka, K. L. (1999), Debris-flow origin for the Simud/Tiu deposit on Mars, *J. Geophys. Res.*, *104*(E4), 8637–8652.

Tanaka, K. L., J. A. Skinner Jr., T. M. Hare, T. Joyal, and A. Wenker (2003), Resurfacing history of the northern plains of Mars based on geologic mapping of Mars Global Surveyor data, *J. Geophys. Res.*, *108*(E4), 8043, doi:10.1029/2002JE001908.

Tanaka, K. L., J. A. Skinner Jr., and T. M. Hare (2005), Geologic map of the northern plains of Mars, *U.S. Geol. Surv. Sci. Invest. Ser., Map SIM-2888*, scale 1:15,000,000, in press.

Tosca, N. J., J. A. Hurowitz, L. Meltzer, S. M. McLennan, and M. A. A. Schoonen (2004), Olivine weathering on Mars: Getting back to basics, *Lunar Planet. Sci.*, *XXXV*, abstract 1043.

Treiman, A. H. (1997), Near-surface geologic units exposed along Ares Vallis and in adjacent areas: A potential source of sediment at the Mars Pathfinder landing site, *J. Geophys. Res.*, *102*(E2), 4219–4229.

Wyatt, M. B., and H. Y. McSween Jr. (2002), Spectral evidence for weathered basalt as an alternative to andesite in the northern lowlands of Mars, *Nature*, *417*, 263–266.

Wyatt, M. B., V. E. Hamilton, H. Y. McSween, P. R. Christensen, and L. A. Taylor (2001), Analysis of terrestrial and Martian volcanic compositions using thermal emission spectroscopy: 1. Determination of mineralogy, chemistry, and classification strategies, *J. Geophys. Res.*, *106*(E7), 14,711–14,732.

Wyatt, M. B., H. Y. McSween Jr., J. E. Moersch, and P. R. Christensen (2003), Analysis of surface compositions in the Oxia Palus region on Mars from Mars Global Surveyor Thermal Emission Spectrometer Observations, *J. Geophys. Res.*, *108*(E9), 5107, doi:10.1029/2002JE001986.

Zuber, M. T. (2001), The crust and mantle of Mars, *Nature*, *412*, 220–227.

J. L. Bandfield, P. R. Christensen, and A. D. Rogers, Department of Geological Sciences, Arizona State University, Campus Box 876305, Tempe, AZ 85287-6305, USA. (deanne.rogers@asu.edu)